

# Parameter Space Exploration for Computational Cardiomyocyte Models, and Application to Investigate Sources of Ventricular Fibrillation



Philip Gemmell  
Computational Biology Group  
University of Oxford

Supervisors:

*Blanca Rodriguez, Kevin Burrage, T. Alexander Quinn*

Summer 2010



## *Acknowledgements*

I would like to thank my supervisors Dr. Blanca Rodriguez, Prof. Kevin Burrage and Dr. T. Alexander Quinn for their support, guidance and unfailing patience with all my efforts over the course of my DPhil so far. I also wish to gratefully acknowledge the help of Dr. Alberto Corrias, Dr. David Spence, Dr. David Abramson and Mr. Blair Bethwaite for their assistance with the Nimrod/G computing grid—without their help and advice, the simulations mentioned in this thesis would not have been possible.



# Contents

<b>1</b>	<b>Introduction</b>	<b>3</b>
<b>2</b>	<b>Background</b>	<b>5</b>
2.1	The Action Potential . . . . .	7
2.1.1	L-Type $\text{Ca}^{2+}$ Current, $I_{\text{CaL}}$ . . . . .	10
2.1.2	Potassium Channels and Currents . . . . .	10
2.1.3	$\text{Na}^+/\text{K}^+$ pump, $I_{\text{NaK}}$ . . . . .	12
2.2	Excitation-Contraction Coupling . . . . .	14
2.2.1	The Calcium Release Unit . . . . .	14
2.2.2	Mechanical Effect of $\text{Ca}^{2+}$ . . . . .	17
2.3	Mechano-Electric Feedback . . . . .	18
2.3.1	MEF Effects On $\text{Ca}^{2+}$ Dynamics . . . . .	18
2.4	Computational Models . . . . .	21
2.4.1	Specific Cell Models . . . . .	22
2.4.2	Model Ion Channel Equations . . . . .	25
2.4.3	Tissue Modelling . . . . .	29
<b>3</b>	<b>Input Parameter Variation for a Computational Cell Model</b>	<b>31</b>
3.1	Computational Methods . . . . .	31
3.2	Analysis of Results . . . . .	34
3.3	2-D Parameter Sweep Results and Discussion . . . . .	38
<b>4</b>	<b>Future Work</b>	<b>43</b>
4.1	Cell-to-Cell Variability . . . . .	43
4.2	Tissue-level Effects of Heterogeneity and Stretch . . . . .	44
4.3	Construction of a Multi-Scale Model . . . . .	46
4.4	Proposed Timeline for Research . . . . .	47

---

# Chapter 1

## Introduction

Computational model simulations and experiments often form a synergistic relationship—the feedback process between computer simulation and experimentation is a cornerstone of computational biology. The results of experimentation often suggest new questions for computational models to address, and in turn *in silico* experiments can help suggest new avenues for *in vitro* research to maximise the return on the experimental investment. Computational models often allow a simpler, cheaper means of investigating relevant biological questions, and can be used to investigate regimes that experimentalists have trouble accessing.

However, many biological problems present a heavy computational task—there are often many different scales and interactions that need to be addressed to produce a complete, biomechanically accurate model, and the consequent modelling often comes with a high computational overhead. The multi-scale nature of the problems found in computational cardiac modelling can be exemplified by the tissue-level phenomena of early and delayed after-depolarisations, and ventricular fibrillation. It is believed that cues for these phenomena can be found in cellular and sub-cellular processes. It is the proposed goal of this research to implement a multi-scale model to fully investigate the multi-scale properties of cardiac tissue, and determine the root causes for these and other phenomena.

It is proposed to do this by constructing a novel computational multi-scale cardiac tissue model, incorporating spatially distributed subcellular components, cellular mechanical effects and influences, and intercellular interactions. It will include the effects of subcellular and cellular physiological variation, and of coupling between the mechanical and electrical environments of the cell. Several different sources of information will be drawn on, including already existing computational cell and tissue models. By complete inclusion of the mentioned effects, it will provide a biologically complete, accurate and realistic model, trained and tested against physiological experimental data, that can be

used to examine all scales, from the subcellular to the tissue. The model can then be used to investigate the response of tissue to pathological conditions, and the role played in this response by individual cells and their subcellular components.

The main focus of the research will be on the repolarisation mechanisms of the cell; consequently, it will be constructed to accurately reproduce biological mechanisms for repolarisation, as opposed to using phenomenological fitting methods wherever possible. The multi-scale nature of the model means it will likely be a computationally intensive model—as such, parallel computing will be used where possible to reduce computing time, and adaptive solving techniques will be used for any ordinary differential equations (ODEs) where required.



# Chapter 2

## Background

Successfully recreating the *in vivo* output of a cardiomyocyte with an *in silico* computational model is a complex, challenging process, with many different choices that can be made during the construction process. Thus, for a model to be constructed in a coherent, efficient manner, four questions must be addressed:

1. What is the goal in creating the model? What research question is the model aimed to address?
2. What are the known mechanisms in the model? How many assumptions have to be made to construct a model?
3. What data are available for constructing, then testing, the model? What data extraction techniques have to be employed, and how will they influence the model?
4. What are the limitations of the computer system to be used for the simulation?

These four questions are not exclusive of each other, and the answer to one will influence the answers to the other three. For the research goals mentioned in the introduction, the creation of a multi-scale model to investigate tissue level repolarisation phenomena, with high fidelity to the actual biological mechanisms in the cell, will require a heavy computational load to be met.

The necessary background for such a project is wide-ranging; the following sections of this chapter will cover the areas identified here:

**Section 2.1, The Action Potential:** AP morphology, reversal/equilibrium potential, membrane ion channel and ion pump properties.

**Section 2.2, Excitation-Contraction Coupling:**  $\text{Ca}^{2+}$  Release Unit,  $\text{Ca}^{2+}$  SR load-release relationship, mechanical effects of  $\text{Ca}^{2+}$  release.

**Section 2.3, Mechano-Electric Feedback:** Stretch-activated channels, mechano-electric feedback effects on  $\text{Ca}^{2+}$  handling,  $\text{Ca}^{2+}$  sparks.

**Section 2.4, Computational Cell Models:** Parameter estimation, stochasticity (intrinsic and extrinsic), whole cell models,  $\text{Ca}^{2+}$  handling models, ODEs for ion channel/pump modelling, tissue modelling.

## 2.1 The Action Potential

The action potential (AP) is the record of the variation of the membrane potential ( $V_m$ ), which is itself the difference in electrical potential between in the intra- and extra-cellular environments. Under normal physiological conditions, it varies from  $\sim -80\text{mV}$  to  $\sim +40\text{mV}$ . It is often regarded as the key measure by which to define the accuracy of a cell model, and as the fundamental output of the cardiomyocyte. However, it is not simply an ‘output’—it is an indicator of, and a participant in, a complex interaction between several different ion channels and exchange mechanisms. The membrane potential is both the consequence of the movement of ions across the membrane, and a key instigator of the openings and closings of the channels and pumps that control this ion movement. However, it should be noted that most ion channels are also sensitive to internal/external ion concentrations, and can display refractory periods after closing/inactivation.

Under physiological conditions, the AP displays a similar shape for all cardiac cell types—a schematic of this shape is shown in Fig. 2.1. The AP can be thought of as having five distinct sections or ‘phases’:

**Phase 0:** Rapid depolarisation. Cell rapidly depolarises from the resting membrane potential of  $\sim -80\text{mV}$  to  $\sim +40\text{mV}$ .

**Phase 1:** Partial repolarisation. Occasionally this rapid repolarisation includes a ‘notch’ in the AP—the cell repolarises to a potential lower than the plateau potential initially, then partially depolarises again to the plateau potential.

**Phase 2:** Plateau. Extended period where membrane potential remains relatively constant due to a balance of inward and outward ion fluxes.

**Phase 3:** Repolarisation of the cell back to its resting potential. Sometimes ‘overshoot’ occurs, resulting in temporary hyperpolarisation of the cell.

**Phase 4:** Steady state. Slow depolarisation occurs in some cells e.g. sino-atrial node.

Some cells have more pronounced phases than others, and this varies both with the pacing regime the cell is subjected to, and with the cell’s spatial location in the heart—sino-atrial node cells have a markedly different AP morphology to ventricular cells, and differences between epi- and endocardial cells in the ventricle have been noted. AP morphology has also been shown to change according to the age of the animal (Carmeliet and Vereecke, 2002).

The initial stage of this research is to investigate the possibility of replacing the input parameter set for several ion channels in a computational model with a parameter space—a number of different parameter sets that produce identical outputs. This will be achieved

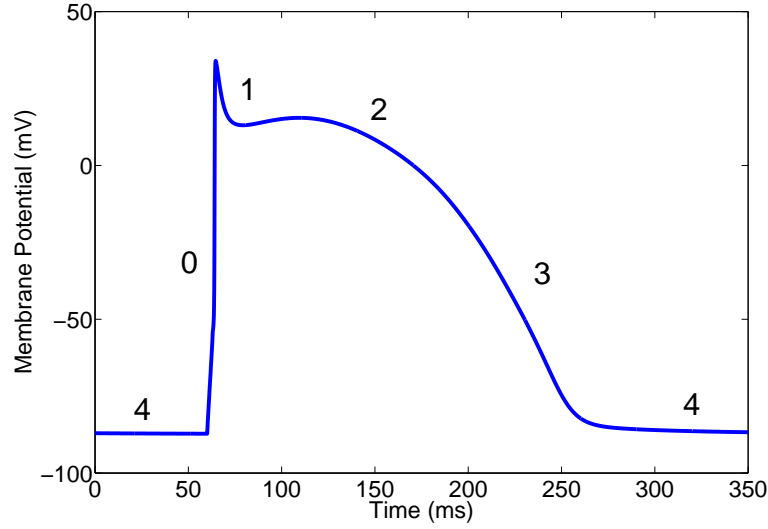


**Figure 2.1:** A schematic of the action potential of a cardiomyocyte, with labels indicating the different phases of the AP.

by exploring the parameter space for six different ion channels which are known to play an important role in the repolarisation of the cell, and determining which values for the parameters produce a viable AP output. The ion channels to be investigated for this variability are:

- L-type  $\text{Ca}^{2+}$  current ( $I_{\text{CaL}}$ )
- Slow delayed  $\text{K}^+$  rectifier current ( $I_{\text{Ks}}$ )
- Rapid delayed  $\text{K}^+$  rectifier current ( $I_{\text{Kr}}$ )
- Inward  $\text{K}^+$  rectifier ( $I_{\text{K1}}$ )
- Sodium-potassium pump ( $I_{\text{NaK}}$ )
- Transient outward current ( $I_{\text{to}}$ )

The first five of these currents play important roles during Phase 3 of the AP, while  $I_{\text{to}}$  is of interest due to its transmural variation in the ventricle. The standard form of the AP, and the output of these six currents during the AP, is shown in Fig. 2.2, to demonstrate the role each current plays in determining the AP.

Their action of membrane ion channels and ion pumps is based on a complicated series of interactions with the membrane potential and the intra- and extra-cellular environment, and a key determinant of this activity is the channel's reversal potential. The reversal potential is defined as the membrane potential at which the free energy of the

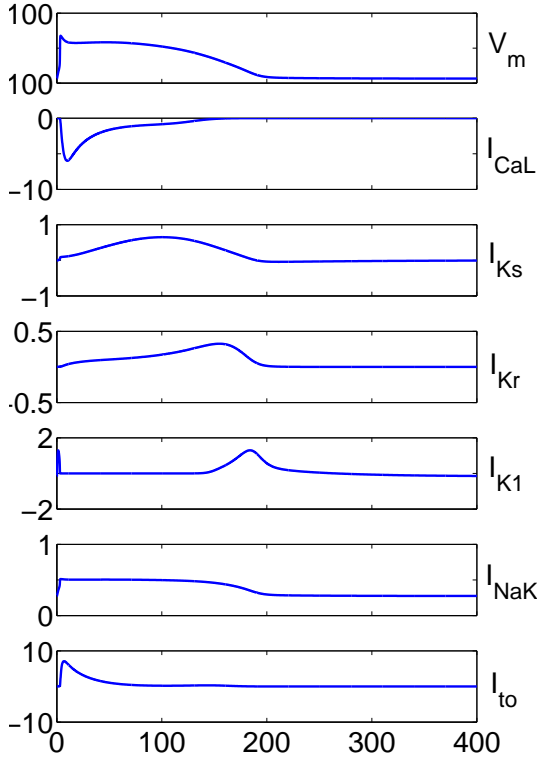


**Figure 2.2:** The membrane potential ( $V_m$ ) during the course of an action potential, and graphs showing the amplitude of six membrane currents ( $I_{CaL}$ ,  $I_{Ks}$ ,  $I_{Kr}$ ,  $I_{K1}$ ,  $I_{NaK}$  and  $I_{to}$ ) during the same period. These data are generated using the model presented in Mahajan et al. (2008).

chemical gradient and the potential gradient are equal but opposite, resulting in no net flow of ions across the membrane through the channel. The simplest expression for this is the Nernst potential, which is given by the Nernst equation:

$$E_\alpha = \frac{RT}{zF} \ln \frac{[\alpha]_o}{[\alpha]_i} \quad (2.1)$$

where, for the ion  $\alpha$ ,  $R$  represents the ideal gas constant,  $T$  the temperature of the system,  $F$  the Faraday constant,  $z$  the valence of the ion, and  $[\alpha]_o$  and  $[\alpha]_i$  represent the extracellular and intracellular concentrations of  $\alpha$  respectively. However, the Nernst potential only considers the case where ions of a single type are present, or if the channel is entirely impermeable to other ions. This is generally not the case (though often the ion channel can be approximated to be 100% selective with good accuracy), and on these occasions the reversal potential is calculated using the Goldman-Hodgkin-Katz equation, also called the Goldman equation, which for  $N$  monovalent positive ionic species and  $M$  negative takes the form

$$E = \frac{RT}{F} \ln \left( \frac{\sum_i^N P_{A_i^+} [A_i^+]_{out} + \sum_j^M P_{B_j^-} [B_j^-]_{in}}{\sum_i^N P_{A_i^+} [A_i^+]_{in} + \sum_j^M P_{B_j^-} [B_j^-]_{out}} \right), \quad (2.2)$$

where  $[\alpha]_o$  is replaced with the sum of all inbound positive and outbound negative ions, and  $[\alpha]_i$  is replaced with the sum of all outbound positive and inbound negative ions, incorporating the permeability  $P_\alpha$  of the channel to the ion  $\alpha$ . It should be noted, therefore, that the reversal potential of a channel, given by the Goldman equation, may be different to the ion's equilibrium potential, which is given by the Nernst equation for that particular ion.

Brief descriptions of the currents to be varied are given below, with details included for their action and kinetics. Most of the information for this section comes from Carmeliet and Vereecke (2002) and Roden et al. (2002).

### 2.1.1 L-Type $\text{Ca}^{2+}$ Current, $I_{\text{CaL}}$

The L-type  $\text{Ca}^{2+}$  current ( $I_{\text{CaL}}$ ) plays an important dual role in the cell—it serves both as an inward current to help maintain the level of depolarisation during Phase 2 of the AP, but also provides the initial  $\text{Ca}^{2+}$  trigger that induces further  $\text{Ca}^{2+}$  release from the sarcoplasmic reticulum (SR); for more details of this release mechanism, see §2.2.

A relatively large depolarisation is needed to open the L-type  $\text{Ca}^{2+}$  channel (LCC):  $-25\text{mV}$  for activation,  $-15\text{mV}$  for  $\frac{1}{2}$ -maximum activation of  $I_{\text{CaL}}$ . Furthermore, the channel can experience two types of inactivation: voltage-based and  $\text{Ca}^{2+}$ -based (Roden et al., 2002). The  $\text{Ca}^{2+}$ -based inactivation is faster, and is due to the submembrane  $\text{Ca}^{2+}$  concentration ( $[\text{Ca}^{2+}]_{\text{sub}}$ ), where the submembrane space is defined as the volume of the cell in close proximity to the membrane, rather than the general cytosolic  $\text{Ca}^{2+}$  concentration ( $[\text{Ca}^{2+}]_i$ )—the two measures of concentration can vary from each other markedly, especially during the first 50ms of the AP. Recovery from inactivation upon hyperpolarisation of the cell is both voltage and  $\text{Ca}^{2+}$  dependent.

The conductance for divalent ions through the channel increases with concentration, and shows saturation—the channel is 500 to 1,000 times more permeable to divalent than monovalent ions. Despite the low permeability of the LCC to  $\text{K}^+$ , the channels remain responsible for a substantial  $\text{K}^+$  current due to the high intracellular  $\text{K}^+$  concentration ( $[\text{K}^+]_i$ ). This  $\text{K}^+$  contribution helps explain why the reversal potential of the  $I_{\text{CaL}}$  is much less positive than expected from the equilibrium potential for  $\text{Ca}^{2+}$  ions: a net influx of  $\text{Ca}^{2+}$  ions occurs when the net current through the channel, including the  $\text{K}^+$  leak, is outward.

### 2.1.2 Potassium Channels and Currents

All of  $I_{\text{Ks}}$ ,  $I_{\text{Kr}}$  and  $I_{\text{K1}}$  are *rectifier* currents—this means that the current-voltage relationship is non-linear, where the current-voltage relationship describes how the current

transmitted through the channel varies according to what electrical potential the channel is at. A channel that passes outward current more easily than inward current is called an *outward rectifier*, with the reverse being an *inward rectifier*.

It should be noted that cardiac cell membranes are highly permeable to  $K^+$  ions, due to inward rectifier  $K^+$  channels being open at rest, as demonstrated by the reversal potential for  $K^+$  ( $V_K$ ) being very close to the resting membrane potential. However,  $V_K$  remains greater than the membrane potential at both rest and at any point during cardiac activity, thus leading to a constant net outward  $K^+$  current. This current leads to a repolarising effect during the AP, and a stabilising effect at hyperpolarised potentials.

### **Slow Delayed $K^+$ Rectifier Current, $I_{Ks}$**

Activation of  $I_{Ks}$  occurs over a wide range of depolarising potentials ( $\frac{1}{2}$ -maximum activation occurs at values varying from  $-13\text{mV}$  to  $+26\text{mV}$ ), with a deactivation time course that varies with species—slow deactivation is seen in guinea pigs, while it is relatively fast in humans and dogs. Along with  $I_{Kr}$ ,  $I_{Ks}$  activates after a short delay following depolarisation, and thus its effect is not seen in Phase 0/1, but rather during Phase 2/3.

### **Rapid Delayed $K^+$ Rectifier Current, $I_{Kr}$**

$I_{Kr}$  activates rapidly at membrane potentials greater than  $-40\text{mV}$ , as its name implies. The time constant of both its activation and deactivation varies among species, as well as being dependent on  $V_m$ —the activation time constant can vary from  $< 100\text{ms}$  to  $500\text{ms}$ , with variation of  $100 - 200\text{ms}$  reported in human ventricular myocytes. The density of  $I_{Kr}$  varies with age, along with the relative importance during repolarisation compared to  $I_{Ks}$ .

### **Inward Rectifier Current, $I_{K1}$**

$I_{K1}$  is a strong inwardly rectifying current—thus the channel helps to help keep the cell at a stable negative resting potential without providing an excessive repolarising current during the plateau of the AP. However, it does still play an important role in the final stages of repolarisation.  $I_{K1}$  channels are present in high density in the ventricle, with their density decreasing in the atria, and  $I_{K1}$  channels being absent in the sino-atrial node. Furthermore, the density of  $I_{K1}$  increases from the foetal stage to the neonatal and adult stage of life.

It should be noted that  $I_{K1}$  has been demonstrated to be affected by the application of stretch and compression to the cell—this is a direct effect of mechanical deformation, and is not due to the resulting changes in ion concentration (Isenberg et al., 2003).

## Transient Outward Current, $I_{to}$

Technically,  $I_{to}$  consists of two currents—the main part, referred to more precisely as  $I_{to1}$  but more commonly as simply  $I_{to}$ , is carried by  $K^+$  ions, while the second, smaller current is referred to by  $I_{to2}$ , and is a  $Ca^{2+}$ -activated chloride ion current. The computational models used in this research assess only  $I_{to1}$ , with  $I_{to2}$  being treated as having a negligible effect on the AP. Thus, for the remainder of this thesis,  $I_{to}$  shall be used to refer solely to  $I_{to1}$ .

$I_{to}$  is a rapidly activated transient outward current which is inactivated during depolarising steps of the AP. Consequently, its main effects are felt during the Phase 1 depolarisation of the AP in atria and ventricular subepicardial cells. Based on kinetics,  $I_{to}$  has both a fast and a slow component ( $I_{to,f}$  and  $I_{to,s}$ , respectively), with the sum of the two being referred to as  $I_{to}$ . Distribution of the two is species dependent, and also varies according to location in the heart—in humans, only  $I_{to,f}$  has been identified in the atria, while both components have been observed in the ventricular midmyocardium.

The recovery from inactivation is very voltage-dependent, occurring faster if the cell is hyperpolarised. It should be noted that the density of  $I_{to}$  varies between different parts of the heart—it is higher in the right ventricular midmyocardium than in the left. Furthermore, transmural differences have been noted, with  $I_{to}$  being present in the subepicardial ventricular tissue, but present only to a negligible degree in subendocardial ventricular tissue. This results in a notch being present in Phase 1 of the AP in subepicardial tissue, which is absent in subendocardial tissue. The density of  $I_{to}$  is also dependent on age, decreasing after birth.

### 2.1.3 $Na^+/K^+$ pump, $I_{NaK}$

The  $Na^+/K^+$  pump is a primary active transport process, acting as it does as an ATPase, using the released energy to move  $Na^+$  and  $K^+$  ions against the concentration gradient. The transportation of the two ions is coupled—for each ATP molecule hydrolysed, three  $Na^+$  ions are moved into the cell, and two  $K^+$  ions are transported in the other direction across the membrane. However, this is variable based on  $V_m$ , and the relative concentrations of ATP, ADP and  $P_i$ .

Due to the unequal number of ions transported across the membrane, the process is *electrogenic*: by the movement of the ions across the membrane, a current ( $I_{NaK}$ ) is generated. As with all ion channels, its activity is in turn affected by the membrane potential it alters. Activation of the pump will hyperpolarise the resting  $V_m$ , or will exert a repolarising effect during the AP.

The density of the pump varies across the heart, with density higher in the ventricles



than in the atria. Furthermore, in the ventricles, the density of the  $\text{Na}^+/\text{K}^+$  pump is greater in subepicardial tissue than in subendocardial tissue.

The pump is maximally stimulated at physiological  $[\text{K}^+]_o$ , but the dissociation constant for the pump for  $[\text{Na}^+]_i$  is  $\sim 10\text{mM}$ , which is close to the physiological range for  $[\text{Na}^+]_i$ . Consequently, the pump's activity is mainly regulated by  $[\text{Na}^+]_i$ , explaining the AP frequency dependence of  $I_{\text{NaK}}$ —an increase in frequency of AP stimulation leads to an increase in  $[\text{Na}^+]_i$ , leading to an enhanced outward pump current, which will lead to hyperpolarisation of the cell.

## 2.2 Excitation-Contraction Coupling

The heart, as an organ, serves to function as an efficient pump to move blood round the body. To do this, it needs to be able to contract in a co-ordinated, repeating manner, and a key component in this process is excitation-contraction coupling (ECC), which is the process by which the electrical system of the heart influences the mechanical output of the heart. ECC presents the link between the AP waveform incident on a cardiomyocyte, and the contraction of that myocyte.

Of all the ions involved in the AP,  $\text{Ca}^{2+}$  is the ion that most explicitly links the electrical and mechanical activity of the cell. It is by  $\text{Ca}^{2+}$ 's release into the cytosolic environment of the cell that the coordinated contraction of the myocyte occurs.

The fundamental unit for  $\text{Ca}^{2+}$  handling in the cell is the  $\text{Ca}^{2+}$  Release Unit (CRU), also referred to as the dyad (Cleeman et al., 1998). These are distributed roughly evenly throughout the cell, in a regular pattern corresponding to the arrangement of T-tubules (invaginations in the cell membrane); the number of CRUs present in the cell has been estimated at being between 10,000 and 100,000 (Cleeman et al., 1998; Bers, 2001; Greenstein and Winslow, 2002; Chen-Izu et al., 2006). This arrangement allows a more uniform influx of  $\text{Ca}^{2+}$  into the cell from the extracellular environment, in turn allowing a more uniform recruitment of CRUs in the cell in response to extracellular input. Computationally, the cell is thus modelled as a 2D grid, with each grid element corresponding to a single CRU. Both the internal structure of a CRU, and an example of its layout in a 2D grid, are shown in Fig. 2.3; a schematic demonstrating the T-tubule and its relation to the SR is shown in Fig. 2.4.

### 2.2.1 The Calcium Release Unit

Physiologically, an individual CRU is a section of the cell, bordered on one edge by cell membrane embedded with L-type  $\text{Ca}^{2+}$  channels (LCC), and containing within a section of the sarcoplasmic reticulum (SR). The SR is a dense network of interconnected tubules and cisternae, which can be subdivided into two components: the network SR (NSR), consisting of the tubular network, and the junctional SR (JSR), consisting of the cisternae. The main function of the SR is to store and, at certain points during the AP, release  $\text{Ca}^{2+}$  ions into the cytosol. The JSR cisternae are located in close proximity to the T-tubules—the space between the two is referred to as the proximal space (or alternatively the dyadic junction). The SR has on its surface between 50 and 250 ryanodine receptor (RyR) channels in each CRU (Chen-Izu et al., 2006; Franzini-Armstrong et al., 1999), which open in response to increased  $\text{Ca}^{2+}$  concentration in the proximal space ( $[\text{Ca}^{2+}]_p$ ), releasing  $\text{Ca}^{2+}$  sequestered in the SR into the cytosol in a process referred to as

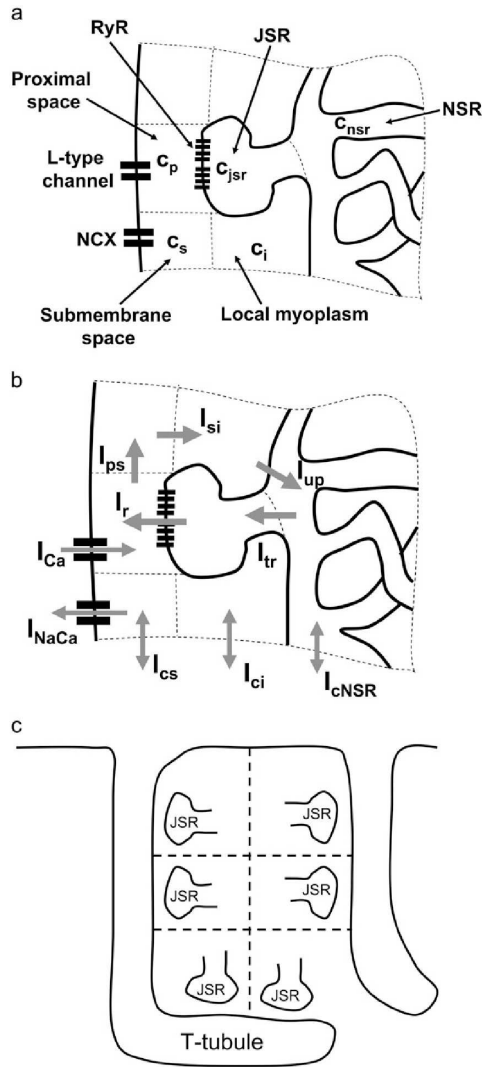


**Figure 2.3:** (a) Structure of an elementary  $\text{Ca}^{2+}$  Release Unit (CRU). Each CRU is considered to consist of several distinct compartments, as shown. (b) Currents in the CRU. (c) Illustration of the arrangement of CRUs with respect to T-tubules in a 2-D grid.

Source: Restrepo et al. (2001)

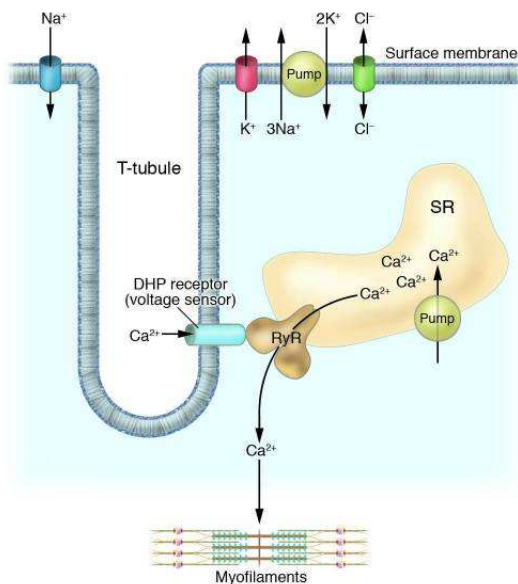


**Figure 2.4:** Schematic demonstrating the proximal location of the SR and the cell membrane due to the invagination of the T-tubule.

Source: Jurkat-Rott and Lehmann-Horn (2005)

$\text{Ca}^{2+}$ -induced  $\text{Ca}^{2+}$  release (CICR). Due to the close proximity of the LCC on the membrane and the RyR channels on the JSR, and consequently the fact that any  $\text{Ca}^{2+}$  influx into the cell via the membrane will be initially concentrated in the proximal space before diffusion can occur, the JSR can be considered as the release point of  $\text{Ca}^{2+}$  from the SR, and the NSR as the point where  $\text{Ca}^{2+}$  is returned to the SR from the cytosol via pumps in an uptake current,  $I_{\text{up}}$ .

Due to the CICR from the SR, the SR  $\text{Ca}^{2+}$  release is the key determinant in the contraction of the cell. The degree of this release is itself determined by the  $\text{Ca}^{2+}$  content of the SR—a non-linear relationship between SR  $\text{Ca}^{2+}$  load and  $\text{Ca}^{2+}$  release is evident (Bassani et al., 1995, 2004). In Restrepo et al. (2001), it is proposed that the SR load-release relationship is due to a buffering mechanism mediated by calsequestrin (CSQN). This proposed mechanism is based on experimental evidence, which indicates an important mechanism for controlling the relationship is modulation of the activity of the RyR channels. It has been noted that the open probability of RyR channels increases upon addition of auxiliary proteins triadin-1/junctin (T/J), but that the probability decreases once again when CSQN is present. Furthermore, the fact that CSQN forms dimers in high  $\text{Ca}^{2+}$  concentrations implies a possible relationship between the three ( $\text{Ca}^{2+}$ , CSQN and T/J) in modulating CICR from the SR. This implied relationship is that the T/J complex binds with the RyR channel, increasing the channel’s open probability. However, the T/J complex binds preferentially with the monomeric form of CSQN, and consequently the open probability of the RyR channels does not increase. However, in high  $\text{Ca}^{2+}$  concentrations, the CSQN dimerises, and is thus unavailable for bonding with the T/J complex, which consequently bonds with RyR channels to increase their open probability, and increase the SR release.

During the resting stage of the cell, the SR  $\text{Ca}^{2+}$  content is determined by the  $\text{Ca}^{2+}$  uptake from the cytosol (largely due to the action of sarco-/endo-plasmic reticulum  $\text{Ca}^{2+}$  ATPase), and  $\text{Ca}^{2+}$  leak from the SR, which is mostly in the form of spontaneous  $\text{Ca}^{2+}$  sparks, a  $\text{Ca}^{2+}$  spark being the ‘activation’ of a single CRU with no AP input. This balance can be either negative (‘rest-decay phenomenon’) as in cats, guinea pigs, rabbits and frogs, or it can be positive (‘post-rest potentiation’) as in humans, mice and rats.

In usual physiological settings, the CRUs across the cell are recruited across the cell almost simultaneously (Restrepo et al., 2001) in response to the extracellular stimulus of decreasing membrane potential at the start of the AP. However, it is possible for a spontaneous  $\text{Ca}^{2+}$  spark to occur. The resulting increase in  $\text{Ca}^{2+}$  concentration in that CRU may in turn activate neighbouring CRUs causing a  $\text{Ca}^{2+}$  wave across a part of the cell, or possibly the whole cell (Chen et al., 2009; Iribe et al., 2009).

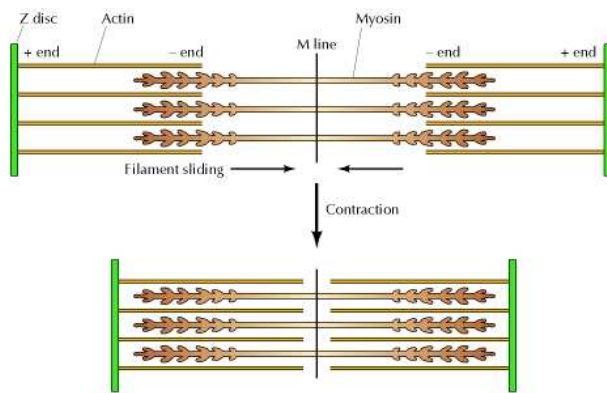


**Figure 2.5:** *Sliding filament model of muscle contraction. When the myosin proteins can move along the actin filament, the result is a shortening of the sarcomere.*

Source: Cooper (2000)

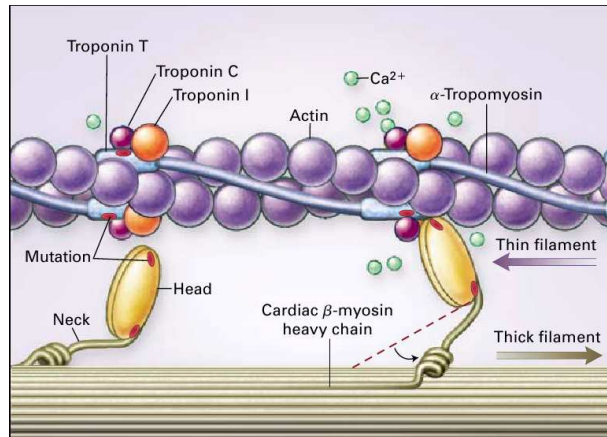


**Figure 2.6:** *Myosin and actin filaments, with the troponin complex and  $\alpha$ -tropomyosin displayed on the actin filament. When  $\text{Ca}^{2+}$  binds to troponin C, a conformational change in the protein complex moves the  $\alpha$ -tropomyosin out of the myosin binding site, allowing actin-myosin interactions to occur to cause muscle contraction.*

Source: Kamisago et al. (2000)

### 2.2.2 Mechanical Effect of $\text{Ca}^{2+}$

Contraction of the cell is achieved by the interaction of two proteins, actin and myosin. These two proteins are arranged into units called sarcomeres, with alternating filaments of each protein. When they interact, the myosin protein ‘walks’ along the actin filament, causing contraction of the sarcomere, and consequently of the cell itself (Fig. 2.5).

As stated,  $\text{Ca}^{2+}$  is the ion that most explicitly links the electrical and mechanical nature of the cell, by mediating the electrical impulse of the AP to the mechanical effect of contraction. It does this by its interaction with a complex of three proteins, collectively referred to as troponin. When the muscle is in its relaxed state, the actin-binding  $\alpha$ -tropomyosin protein is locked in place on the actin filament by two of the troponin complex proteins, troponin I and troponin T. This blocks binding between the myosin protein and the actin filament, consequently preventing contraction. However, when  $\text{Ca}^{2+}$  is released from the SR,  $[\text{Ca}^{2+}]_i$  increases, and the binding between  $\text{Ca}^{2+}$  and a third troponin protein, troponin C, similarly increases in rate. This binding produces a conformational change in the complex, moving the  $\alpha$ -tropomyosin out of the way of the myosin binding site, allowing the myosin-actin interaction that leads to the contraction of the sarcomere, in turn leading to contraction of the myocyte, and consequently the muscle tissue generally (Fig. 2.6).

## 2.3 Mechano-Electric Feedback

The impact of the electrical properties of the cell on the mechanical properties of the cell, referred to as ECC, is only one side of the relationship—mechanical properties are also known to influence the electrical properties of the cell, in a process referred to as mechano-electric feedback (MEF). The effects of stretch and strain on the electrical environment of the system have important implications for cardiac function, and thus a correct understanding of MEF is vital for the construction of accurate cardiac models.

Important work has already been conducted in elucidating the means and mechanisms of MEF—patch clamp experiments have identified non-specific, stretch-activated ion channels (SACs) (Sachs et al., 1991) which, as the name implies, provide a direct means of mediating the effect of mechanical stretch to a measureable electrical output. The possible role in SACs in ventricular fibrillation has already been investigated (Gurev et al., 2006). Additionally, evidence exists that voltage-gated channels are sensitive to mechanical pressure—indeed, it can be argued that this is a natural consequence of a membrane channel protein’s interactions with its membrane environment (Morris and Laitko, 2005).

With regards  $\text{Ca}^{2+}$  dynamics, Matsuda et al. (2008) demonstrates an increase in the open probability of LCC, and consequently an increase in  $I_{\text{CaL}}$ , in rabbit atrial and sinoatrial node cells in response to cell swelling at every membrane potential tested. However, Belus and White (2003) found no evidence of stretch impacting  $I_{\text{CaL}}$  in guinea pig ventricular myocytes. Furthermore, chamber dilation is now implicated as playing a major role in the development of atrial fibrillation (Kohl et al., 2005).

### 2.3.1 MEF Effects On $\text{Ca}^{2+}$ Dynamics

On a general level, the effects of mechanical stretch on  $\text{Ca}^{2+}$  dynamics have been noted (Calaghan and White, 1999)—through  $\text{Ca}^{2+}$  mechanisms, stretch has been shown to alter AP configuration, increase the risk of arrhythmogenesis and increase the rate of beating in the SAN, but the exact cellular mechanisms for these effects is still under investigation. Relatively little work has been conducted on investigating the effects of stretch on cellular  $\text{Ca}^{2+}$  processes—for instance, most work on  $\text{Ca}^{2+}$  spark dynamics has been conducted on mechanically-unloaded cells. Research thus far indicates that axial stretch reduces the overall SR  $\text{Ca}^{2+}$  load in guinea pig cardiomyocytes (Iribe and Kohl, 2008), which would lead to a consequent reduction in  $\text{Ca}^{2+}$  available for recruitment in  $\text{Ca}^{2+}$  sparks. However, individual  $\text{Ca}^{2+}$  spark rate was not recorded in this work. It has also been demonstrated (Petroff et al., 2008) that axial stretch increases the  $\text{Ca}^{2+}$  spark rate in rat cardiomyocytes via a nitric oxide mediated pathway, but this result was only observed

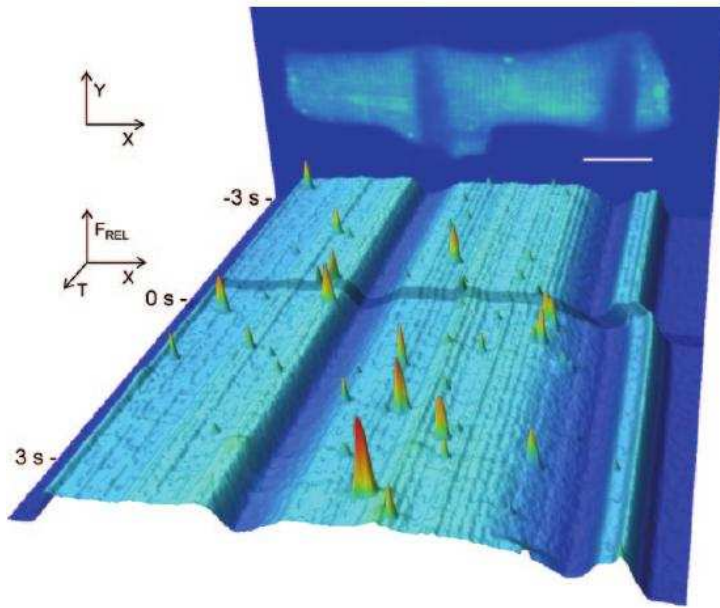


**Figure 2.7:** Time course of relative Fluo-4 signal intensity in rat ventricular resting cardiomyocyte, illustrating the increase in spontaneous  $\text{Ca}^{2+}$  spark rate after the application of half-cell stretch. The panel at the back shows an image of the cell, averaged from 10 confocal XY scans, before stretch application. Low signal intensity areas overlapping the cell body reveal carbon fibre positions before and during stretch. Source: Iribe et al. (2009)

after extended exposure to the stretch (10 minutes), and thus did not illuminate the acute response to stretch.

To that end, Iribe et al. (2009) directly investigates the acute effect of axial stretch on  $\text{Ca}^{2+}$  spark rate, and investigates the possible mechanisms that mediate the effect. Carbon fibres were used to apply whole-cell and half-cell stretch of  $8.01 \pm 0.94\%$  to an isolated rat ventricular cardiomyocyte. XY confocal imaging was then used to image the cell, which had been prepared using Fluo-4 to allow fluorescent imaging of  $\text{Ca}^{2+}$  sparks.

The experiments established that application of axial stretch causes an acute increase in the  $\text{Ca}^{2+}$  spark rate (to  $130.7 \pm 6.4\%$  of initial levels in whole cell stretch,  $128.2 \pm 7.2\%$  in the stretched section of partial cell stretch) within 5 seconds of the application of stretch, followed by a return to initial levels ( $104.4 \pm 5.1\%$ ) within 1 minute. The dynamic properties of individual sparks (i.e. spark amplitude, time to peak amplitude, decay time constant) are not affected. The partial cell stretch experiments demonstrated that the increase in  $\text{Ca}^{2+}$  spark rate is a local phenomenon—the observed increase in  $\text{Ca}^{2+}$  spark rate occurred only in the stretched segment, with  $\text{Ca}^{2+}$  spark rate statistically unchanged ( $91.1 \pm 6.7\%$ ) in the unstretched section (Fig. 2.7).

Several possible explanations for this observed phenomenon are considered by Iribe et al. (2009). These include:

- The transient increase in  $\text{Ca}^{2+}$  spark rate is due to a transient increase in  $\text{Ca}^{2+}$  concentration in the proximal space. This increase in concentration could be due either to a general spatial rearrangement of the cell, or merely a compression of the proximal space in response to the stretch. The  $\text{Ca}^{2+}$  spark rate returns to control levels as diffusion from the proximal space to the bulk cytosol ‘normalises’ the concentration

to control levels.

- Transmission of stretch from the cell surface to the T-tubular SR complex of the CRU by cytoskeletal structures, which consequently affects the mechanisms of  $\text{Ca}^{2+}$  release.
- Extra-cellular  $\text{Ca}^{2+}$  enters the cell by activation of SACs, or other mechanically activated channels/transporters (Inoue et al., 2006; Kupittayanant et al., 2006), and thus induces CICR from CRUs.
- Involvement of nitric oxide (NO) in the acute response of  $\text{Ca}^{2+}$  spark rate to stretch (Petroff et al., 2008).

Several experiments were conducted by Iribe et al. (2009) to determine if any of these hypotheses is correct. The partial cell stretch experiments demonstrated the effect to be local in the cell, and not global throughout the cell—this argues against a global mechanism being responsible for the change in spark rate, such as membrane depolarisation. They furthermore discounted spatial rearrangement of the cell as the potential cause, citing that 8% axial stretch equates to only  $\sim 4\%$  radial compression (however, no simulations were conducted to confirm this theory). Cell stretch was conducted in the presence of the SAC blocker GsMTx-4—no effect on the results of stretch was seen, implying SACs play a negligible role in mediating the change. The increase in sparking rate is still evident if the stretch is performed while the cell is in a  $\text{Ca}^{2+}$ -free extracellular medium, implying no link between the increase in the  $\text{Ca}^{2+}$  spark rate and the extra-cellular environment. Furthermore, possible involvement of the NO mechanism postulated in Petroff et al. (2008) was investigated by performing cell stretch after the cell had been pre-incubated in  $N^G$ -nitro-L-arginine methyl ester to block NO-synthase—no effect on the stretch effect was observed, implying the acute increase in  $\text{Ca}^{2+}$  spark rate is independent of any NO-related mechanism.

The authors suggest an involvement of microtubules in increasing the open probability of the RyR channels—this would initially increase the spark rate, leading to a depletion of  $[\text{Ca}^{2+}]_{\text{SR}}$ . Due to the SR load-release relationship, the authors argue that this depletion would subsequently allow spark rate to return to near control levels. To test this hypothesis, stretch experiments were conducted after the cell had been pre-incubated with colchicine, which inhibits microtubule formation. Pre-stretch spark rate is unaffected by this application, but no acute stretch effects are observed, implying the mechanism communicating the stretch effect requires microtubule involvement. They argue further that the distance between microtubules and the T-tubule-SR membrane complex is comparable to other instances where a mechanical link has been demonstrated, and thus it is reasonable to suggest the involvement of the microtubule network in this instance.



## 2.4 Computational Models

Many models have been proposed to study various properties of cardiomyocytes in response to various experimental regimes (Hutter and Noble, 1960; Noble, 1960; Luo and Rudy, 1994a,b; Sherifaw et al., 2003; Shannon et al., 2004; Rudy and Silva, 2006; Restrepo et al., 2001; Mahajan et al., 2008; Chen et al., 2009). They have proven remarkably successful, offering a variety of insights into biological and biomechanical properties of the cell, and have helped pave the way for further physiological experiments to confirm or deny theories that would otherwise not have been posed.

However, many models suffer from the problem of gathering enough experimental data to sufficiently define all the input parameters needed. Consequently, a model may use parameters from any one of the following sources:

- Experimentally verified parameters from whole cell experiments for the species in question.
- Experimentally verified parameters from a cloned ion channel. The channel need not be derived from the same species as the model, as long as it can be confidently stated that the ion channel is present in the model species.
- Parameters that are not independently verified, but their choice is determined by a phenomenological fit of the model output to experimental data.

Often the exact source of a parameter is not emphasised, and it is often forgotten that some of the parameters in the model are chosen due to their giving the correct model response rather than any firmer experimental footing. It is then often the case that all model parameters are treated as epistemologically equivalent, with no caveats made for the source of the parameter value. Furthermore, it is implicitly assumed that there is a single value a parameter can take—subsequent models may alter the particular value of a particular parameter, but there is always one, single value.

Unless stochasticity in the system is taken into account, this single parameter set will produce a single, unchanging output. However, the experimental AP output from a cardiomyocyte taken from a given section of tissue is not constant—cell-to-cell and beat-to-beat variability have already been noted in the literature (Walmsley et al., 2010). This variation is an example of the natural variation experienced in almost all biological systems—it is rare to find a biological system that will give consistent, identical output to consistent, identical input. In the case of cardiomyocytes, this variation ranges from species variation (Romero et al., 2010), to variation between individuals within a species, to variation between cells within the same tissue, even down to temporal variation for the same cell (Walmsley et al., 2010). This variation can often be traced back to the

stochasticity inherent in many cell processes, where the number of interacting entities is small enough that random fluctuations play an important role in determining the outcome.

At this stage, it is useful to introduce a distinction between two different stochastic processes—intrinsic and extrinsic noise. As the names imply, intrinsic noise is due to stochasticity within the system, while extrinsic noise has its causes in events exterior to the system. The intrinsic noise is here represented by two phenomena. The first is mentioned in §2.2.1: spontaneous  $\text{Ca}^{2+}$  sparks. These  $\text{Ca}^{2+}$  sparks are due to stochastic fluctuations in either the  $\text{Ca}^{2+}$  concentration in the proximal space, or in fluctuations in the open/close state of RyR channels, or a combination of the two. The second phenomenon is that of variation in input parameter values—any difference between any two measurements of a given input parameter. By taking multiple measurements, this intrinsic noise effect can be minimised, but it is important to realise that, though all measurements of a particular parameter will be centred around a given, mean value, that does not mean a particular instantiation of the parameter will take that mean value.

### 2.4.1 Specific Cell Models

The evolution of many cell models can generally be traced back along a curve of improvement and specialisation, and has a long history extending back at least as far as 1960 (Hutter and Noble, 1960; Noble, 1960). However, the general cell model presented in Luo and Rudy (1991) is the seed that most of the models used in this thesis are based on (though this model in turn is based on earlier work). This model is a mathematical model of a single ventricular cardiac cell action potential using the Hodgkin-Huxley formulation (Hodgkin and Huxley, 1952) to model  $\text{K}^+$  and  $\text{Na}^+$  ion currents. Luo & Rudy subsequently built upon this model (Luo and Rudy, 1994a,b) to include a more in-depth formulation of intracellular  $\text{Ca}^{2+}$  dynamics. This model (hereafter referred to as the LR model) reflected the realisation that  $\text{Ca}^{2+}$  dynamics can play an important role in fast pacing regimes—as models were designed to simulate high heart rates, to subsequently investigate tachycardia and arrhythmogenesis, more details of the  $\text{Ca}^{2+}$  handling systems of the cell needed to be incorporated into the model.

The LR model is expanded upon in Shannon et al. (2004) (hereafter referred to as the Shannon model), which uses more recently available data regarding excitation-contraction coupling (ECC) to improve the accuracy of the model. For instance, the coupling between SR  $\text{Ca}^{2+}$  load and  $\text{Ca}^{2+}$  release is included, together with reformulation of the  $\text{Ca}^{2+}$  modelling system to include a submembrane compartment to better account for the different  $\text{Ca}^{2+}$  concentrations present throughout the cell. This model was subsequently revised, mainly in terms of the  $\text{Ca}^{2+}$  handling mechanisms of the LCC and  $\text{Ca}^{2+}$  cycling compo-

ment for  $\text{Ca}^{2+}$  movement to and from the SR, by Mahajan et al. (2008). A seven-state pseudo-Markov model of  $I_{\text{CaL}}$  is incorporated into the model (hereafter referred to as the Mahajan model), consequently successfully modelling the dynamics of the cardiac AP and the intracellular  $\text{Ca}^{2+}$  cycling at high heart rates. Furthermore, the Mahajan model also correctly demonstrates the development of alternans in both APD and  $[\text{Ca}^{2+}]_i$  at rapid heart rates.

The LR model is not able to successfully reproduce the graded relationship between  $I_{\text{CaL}}$  and SR  $\text{Ca}^{2+}$  release, due to the fact it uses a so-called ‘common pool model’, as termed by Stern (1992). Stern noted that there is a discrepancy between the ‘all-or-nothing’ response of the RyR channels to  $\text{Ca}^{2+}$  influx, and the linear dependence of the SR  $\text{Ca}^{2+}$  release on  $I_{\text{CaL}}$ . In the paper, it is hypothesised that this discrepancy can be overcome by introducing a compartmentalised model for the  $\text{Ca}^{2+}$  dynamics. In a compartmentalised model, the different spatial sections of the cell are not treated as spatially distinct, but rather as coupled compartments of the model, with relationships such as diffusion treated as interactions between the compartments with no explicit mention of spatial organisation. As such, Stern points out that stochastic recruitment of local release fluxes can be combined to give the total  $\text{Ca}^{2+}$  release, with a small cluster of LCC coupled to a cluster of RyR channels via a local pool of  $\text{Ca}^{2+}$ ; the result is a graded release of SR  $\text{Ca}^{2+}$  in response to  $I_{\text{CaL}}$ . Stern’s hypothesis was later validated by high resolution confocal imaging, demonstrating that the rise in  $\text{Ca}^{2+}$  across the cell is due to the summation of many local  $\text{Ca}^{2+}$  sparks (Cleeman et al., 1998).

Sherifaw et al. (2003) expanded the model of Stern (1992) in a  $\text{Ca}^{2+}$  dynamics model, with separate compartments for the submembrane space and the bulk cytosol, and by including the SR load-release dependence observed experimentally (Bassani et al., 1995, 2004); however, this dependence was fitted phenomenologically, with no physiological basis for the fit (Fig. 2.8). The model is successful in reproducing the experimental observations of CTA at high pacing rates independent of APD alternans (Chudin et al., 1999), thus demonstrating the SR load-release relationship as a mechanism for instability in the  $\text{Ca}^{2+}$  transient arising independently of instability in the APD. Another mechanism cited is a dependence on the diastolic  $[\text{Ca}^{2+}]_i$ , which mediates its effect through  $\text{Ca}^{2+}$ -induced inactivation of the LCC.

However, the model’s proposed mechanism displays diastolic SR  $\text{Ca}^{2+}$  alternans whenever there is CTA, which is disputed by experimental work in Picht et al. (2006)—this suggests there is an alternative mechanism for the genesis of CTA without SR  $\text{Ca}^{2+}$  content alternans. To this end, Restrepo et al. (2001) produces a model that includes CSQN buffering of the SR  $\text{Ca}^{2+}$  content as described in §2.2.1. This model is a linear  $\text{Ca}^{2+}$  handling model that, when paced with a periodic, rapid AP, correctly reproduced CTA, thus

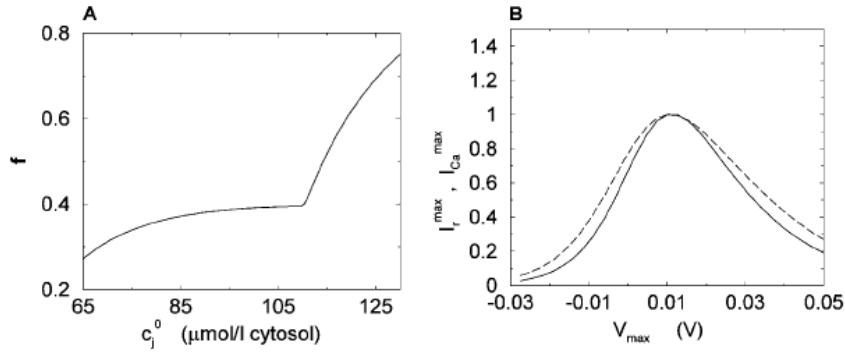


**Figure 2.8:** (A) Fractional SR release  $f$  versus initial SR load  $c_j^0$ . For all points, initial conditions are  $[Ca^{2+}]_{sub}=[Ca^{2+}]_{cytosol}=0.1\mu M$ ,  $f(0)=1$ ,  $d(0)=0$ ,  $q(0)=0.8$ ,  $I_r(0)=0\mu Ms^{-1}$ , where  $d$  describes the voltage-dependant activation of the LCC,  $q$  describes the  $Ca^{2+}$ -induced inactivation of the LCC and  $I_r$  denotes the total flux due to  $Ca^{2+}$  sparks. (B) Relationship between peak  $I_{CaL}$  and peak SR flux. The solid line is  $I_r^{max}(V_{max})$ , and the dashed line is  $I_{CaL}^{max}(V_{max})$ . Both curves have been normalised to their peak values. The initial conditions are identical to those in (A), except that the initial total SR load is fixed at  $[Ca^{2+}]_{SR}=100\mu mol l^{-1}$  cytosol.

Source: Sherifaw et al. (2003)

demonstrating a link between the microscopic properties and the whole cell behaviour of the cell. The model is notable for introducing a spatial architecture for CRUs—it is not a compartmental model, and instead makes explicit account of the spatial environment of the cell, and the spatial interaction between different spatial components. The cell is modelled as a 3-D grid with  $\sim 20,000$  elements, with each grid element corresponding to a single CRU.

The models by Stern (1992), Sherifaw et al. (2003) and Restrepo et al. (2001) are all  $Ca^{2+}$  dynamics models—they model the  $Ca^{2+}$  handling processes of the cell, but do not model the other ionic processes that occur. For a more detailed investigation of cell properties, a whole cell model needs to be used, which models the dynamics of known cellular ion transport processes. A whole cell model consequently has the AP as a dynamic component within the model—it is not an input into the model, but rather a cause of and result of the complex interactions between ion concentrations. This makes the resulting model more computationally expensive, but allows for a more detailed assessment to be made of the accuracy of the parts of the model with their interactions now included.

In Chen et al. (2009), the Mahajan cell model was combined with the  $Ca^{2+}$  handling model from Restrepo et al. (2001) to produce a novel whole cell, spatially distributed model (hereafter referred to as the Chen model). In this model, the CSQN buffering present in the original Restrepo model is dropped due to a different experimental regime being under consideration, while allosteric coupling between adjacent RyR channels in

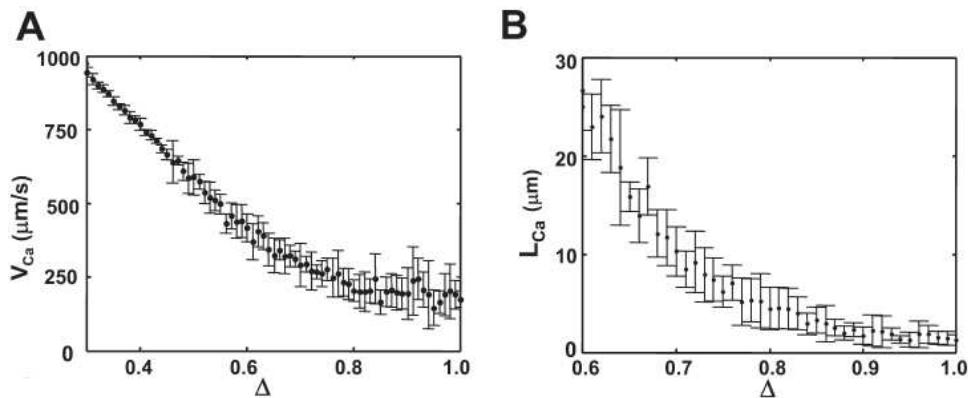


**Figure 2.9:** *Demonstration of the link between the subcellular CRU mechanism and the cellular  $\text{Ca}^{2+}$  wave speed and propagation distance. Depending on the level of coupling between adjacent RyR channels (represented by  $\Delta$ , with  $\Delta = 1.0$  being the physiological value, and  $\Delta < 1.0$  representing reduced coupling), the wave speed and propagation distance of a  $\text{Ca}^{2+}$  wave moving through the cell is affected.*

*Source: Chen et al. (2009)*

the CRU is introduced. This coupling is demonstrated to have a profound impact on the  $\text{Ca}^{2+}$  wave speed and distance, as well as the  $I_{\text{CaL}}$  influx required to initiate a  $\text{Ca}^{2+}$  spark in a CRU. The paper is notable for demonstrating a link between the subcellular  $\text{Ca}^{2+}$  dynamics of the CRU and the cellular AP form (Fig. 2.9). Using the subcellular resolution granted by the spatial arrangement of the Restrepo model, and linking it to the ion channel dynamics from the Mahajan model, the Chen model is able to trace any changes in AP morphology, and other cellular phenomena, back to their subcellular causes.

### 2.4.2 Model Ion Channel Equations

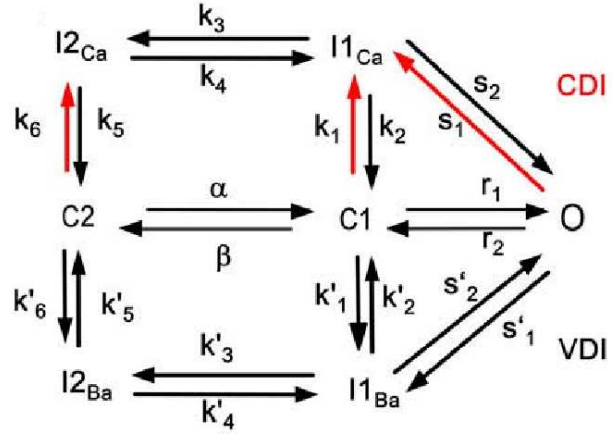
The Mahajan model uses an extensive set of ODEs to model the membrane ion channels and ion pumps, with a pseudo Markov model representing the LCC dynamics. A brief description of the ODEs for the ion channels that are varied in the studies of this DPhil is given below; for full details for the model, the reader is referred to Mahajan et al. (2008).

The L-type  $\text{Ca}^{2+}$  channel dynamics are modelled using a minimal seven-state Markovian model incorporating closed, open and inactive states for the channel (Fig. 2.10). The resulting equation to describe  $I_{\text{CaL}}$  is given by

$$I_{\text{CaL}} = -2 \frac{Fv}{C_m} g_{\text{Ca}} P_o i_{\text{Ca}}, \quad (2.3)$$

where  $F$  is Faraday's constant,  $v$  is the cytosol volume,  $C_m$  is the membrane capacitance,  $g_{\text{CaL}}$  the strength of the  $\text{Ca}^{2+}$  current flux,  $P_o$  the probability the channels are open, and  $i_{\text{Ca}}$  is the unitary current through LCC (which changes with voltage). Universal

**Figure 2.10:** Seven-state Markov model for the LCC. There are two closed states, four inactive states and one open state. The lower inactive states are voltage-dependent, while the upper inactive states are  $\text{Ca}^{2+}$ -dependent. Source: Mahajan et al. (2008)



Parameter	Definition	Value
$F$	Faraday's constant	$93,485.339 \text{ C mol}^{-1}$
$C_m$	Cell capacitance	$3.1 \times 10^4 \mu\text{F}$
$v$	Cell cytosol volume	$2.58 \times 10^{-5} \mu\text{l}$
$R$	Ideal gas constant	$8.314472 \text{ J mol}^{-1} \text{ K}^{-1}$
$\gamma\rho$	SAC peak current density	$0.75 \text{ mScm}^{-2}$
$V_r$	SAC reversal potential	$-10 \text{ mV}$
$K$	SAC parameter defining current when cell unstretched	110
$\alpha$	SAC parameter defining sensitivity to stretch	14.7

**Table 2.1:** Values of constants in membrane ion channel equations.

constants and those parameters that are universal for all ionic equations are given in Table 2.1, while the values for peak conductances are given in Table 2.2.

The modelling equations used for  $I_{\text{Kr}}$  are based on the original formulation in the LR model, but with modifications (due to Puglisi and Bers (2001)) that were originally implemented in the Shannon model.  $I_{\text{Kr}}$  is thus modelled by

$$I_{\text{Kr}} = g_{\text{Kr}} \sqrt{\frac{[K^+]_o}{5.4}} x_{\text{Kr}} R(V_m)(V_m - E_K), \quad (2.4)$$

where  $R(V_m)$  represents the inactivation gate dependence for  $I_{\text{Kr}}$ , and  $E_K$  represents the reversal/equilibrium potential for  $\text{K}^+$ .

The  $I_{\text{Ks}}$  model equation is

$$I_{\text{Ks}} = g_{\text{Ks}} x_{s1} x_{s2} q_{\text{Ks}} (V_m - E_{\text{Ks}}), \quad (2.5)$$

where  $g_{\text{Ks}}$  represents the peak  $I_{\text{Ks}}$  conductance,  $x_{s1}$  and  $x_{s2}$  represent gating variables for the channel,  $q_{\text{Ks}}$  models the dependence of the channel on  $[\text{Ca}^{2+}]_i$ , and  $E_{\text{Ks}}$  represents the reversal potential for the channel (it should be noted that this is *not* the reversal potential

Parameter	Definition	Value
$g_{CaL}$	Strength of the $Ca^{2+}$ current flux	$182 \text{ mmol cm}^{-1} C^{-1}$
$g_{Ks}$	Peak $I_{Ks}$ conductance	$0.1386 \text{ mS}\mu F^{-1}$
$g_{Kr}$	Peak $I_{Kr}$ conductance	$0.0125 \text{ mS}\mu F^{-1}$
$g_{K1}$	Peak $I_{K1}$ conductance	$0.3 \text{ mS}\mu F^{-1}$
$g_{NaK}$	Peak $I_{K1}$ conductance	$1.5 \text{ mS}\mu F^{-1}$
$g_{to,f}$	Peak $I_{to,f}$ conductance	$0.11 \text{ mS}\mu F^{-1}$
$g_{to,s}$	Peak $I_{to,x}$ conductance	$0.04 \text{ mS}\mu F^{-1}$

**Table 2.2:** Values of peak conductances and strength of flux for ion channels. The value for  $g_{CaL}$  is in  $\text{mmol cm}^{-1} C^{-1}$ , meaning it is a measure of the flux of ions moving across the cell membrane per cm thickness of membrane, per coulomb charge on the membrane. The other peak conductances, on the other hand, are in units of  $\text{mS}\mu F^{-1}$ , meaning it is a unit of conductance of channel per unit capacitance. The reason for this difference lies in the Markov formulation of  $I_{CaL}$ , meaning the  $Ca^{2+}$  flow through LCC is treated as a diffusive flow in terms of concentration, while the other channels are abstracted as an electric current.

for  $K^+$ —this difference is due to the channel’s permeability to  $Na^+$ ). The formulation of  $I_{Ks}$  is based on the original equation set out in Luo and Rudy (1994a) with modifications found in Shannon et al. (2004) to account for experimental data from Tohse (1990), with further modifications to the  $Ca^{2+}$  dependence to fit with dynamic restitution data. The gating variables vary according to differential equations, with parameters that vary according to the value of  $V_m$ .

The  $I_{K1}$  current is modelled in the same way as in the LR and Shannon models, by

$$I_{K1} = g_{K1} \sqrt{\frac{[K^+]_o}{5.4}} \frac{A_{K1}}{A_{K1} + B_{K1}} (V_m - E_K), \quad (2.6)$$

where  $g_{K1}$  represents the maximum conductance of the channel,  $[K^+]_o$  represents the extracellular  $K^+$  concentration, and  $\frac{A_{K1}}{A_{K1} + B_{K1}}$  represents the steady state for the inactivation gate for the  $I_{K1}$  channel. However, as noted in Gurev et al. (2006),  $I_{K1}$  is directly affected by mechanical deformation. The resulting change to  $I_{K1}$ , and the outwardly rectifying  $K^+$  current ( $I_{Ko}$ ), is modelled in that paper by

$$\Delta I_{K+} = 5.25L(\lambda)[I_{K1(\text{stretched})} + I_{Ko(\text{stretched})} - I_{K1(\text{unstretched})} - I_{Ko(\text{unstretched})}], \quad (2.7)$$

where the current magnitude depends on stretch according to

$$L(\lambda) = \frac{1}{1 + Ke^{-\alpha(\lambda-1)}}. \quad (2.8)$$

The parameter that modulates  $L$ ,  $\lambda$ , represents the stretch ratio that corresponds to the

strain in the fibre direction:  $\lambda = \sqrt{2E_{ff} + 1}$ , where  $E_{ff}$  is a component of the Lagrangian strain tensor, corresponding to the fibre direction.  $I_{K1(\text{stretched})}$  represents the inwardly rectifying  $K^+$  current and  $I_{Ko(\text{stretched})}$  the outwardly rectifying  $K^+$  whole cell current measured at 22% local stretch of the cell. The scaling factor 5.25 ensures  $5.25L(\lambda) = 1$  at  $\lambda = 1.22$  (22% stretch).

Like the equations for  $I_{K1}$ , the equations for  $I_{NaK}$  are the same as those found in the LR model:

$$I_{NaK} = g_{NaK} f_{NaK} \left( \frac{1}{1 + (12\text{mM}/[\text{Na}^+]_i)} \right) \left( \frac{[\text{K}^+]_o}{[\text{K}^+]_o + 1.5\text{mM}} \right). \quad (2.9)$$

In the above equation,  $f_{NaK}$  is a voltage-dependent parameter.

The formulation for  $I_{to}$  used here, taking separate account of  $I_{to,f}$  and  $I_{to,s}$ , was originally implemented in Bassani et al. (2004), using data from Wang et al. (1999) for  $I_{to,s}$ , and represents the two components as

$$I_{to,f} = g_{to,f} X_{to,f} Y_{to,f} (V_m - E_K), \quad (2.10)$$

$$I_{to,s} = g_{to,s} X_{to,s} (Y_{to,s} + 0.5R_s^{\text{inf}}) (V_m - E_K). \quad (2.11)$$

In these equations,  $X_{to,x}$  and  $Y_{to,x}$  represent the voltage-dependent terms of current activation and inactivation, respectively, and  $R_s^{\text{inf}}$  accounts for the slow recovery from inactivation.  $I_{to}$  is the sum of these two currents, and it is this sum that is scaled in the experimental protocol discussed in §3.

The model that is proposed to be constructed is to take into account the effects of stretch and strain on the system. One of the means of doing this is to include terms to model SACs. To this end, the formulation from Gurev et al. (2006) will be followed, itself based on the work from Zabel et al. (1996). The current density of the SACs is modelled by

$$I_{\text{SAC}} = -L(\lambda) \times [\gamma \rho (V_m - E_{\text{SAC}})], \quad (2.12)$$

where  $\gamma$  represents the single channel conductance,  $\rho$  the channel density,  $E_{\text{SAC}}$  the reversal potential, and  $K$  and  $\alpha$  are parameters controlling the amount of current at tissue reference length and the sensitivity to stretch.

It should be noted that, in constructing the rabbit ventricular myocyte model of Mahajan et al. (2008), many different sources of information were used. Closer examination of these sources serves to emphasis the caution that must be used in using models of this type—some papers use data designed for rabbit, canine or human myocytes, and some for atrial myocytes. However, due to the scarcity of available, relevant data, parameters must often be pooled to allow construction of a full, if flawed, model.



### 2.4.3 Tissue Modelling

The most common model to simulate propagation of electrical excitation in cardiac tissue is the *bidomain equation* (Keener and Sneyd, 1998), which represents the intra- and extra-cellular environments as being continuous and intertwined at all points in the tissue. The consequence of this representation is that each point has both an intracellular potential  $\phi_i$  and an extracellular potential  $\phi_o$ . The membrane potential is, as stated previously, the difference between these:

$$V_m = \phi_i - \phi_o. \quad (2.13)$$

The bidomain equations are coupled differential equations, based on a reaction-diffusion model of ion flux, with the application of conservation of ions and charge throughout the domain. The resulting equations covering the domain  $\Omega$  are

$$\beta \left( C_m \frac{\partial V_m}{\partial t} + I_{\text{ion}}(\boldsymbol{\eta}, V_m) \right) - \nabla \cdot (\sigma_i \nabla \phi_i) = I_{\text{stim},i} \quad \text{in } \Omega, \quad (2.14)$$

$$\nabla \cdot (\sigma_o \nabla \phi_o + \sigma_i \nabla \phi_i) = I_{\text{stim},o} \quad \text{in } \Omega, \quad (2.15)$$

where  $\beta$  is the membrane surface to volume ratio,  $C_m$  is the specific membrane capacitance, and  $I_{\text{stim},i}$  and  $I_{\text{stim},o}$  are stimulus currents applied to the intra- and extra-cellular space respectively.  $I_{\text{ion}}$  is the sum of the ionic currents from the extracellular to the intracellular domain, and depends on the cell model being used. The variable  $\boldsymbol{\eta}$  also depends on the cell model choice, being a vector containing the state variables for the cell electrophysiology model. It varies according to

$$\frac{\partial \boldsymbol{\eta}}{\partial t} = \mathbf{f}(\boldsymbol{\eta}, V_m), \quad (2.16)$$

where  $\mathbf{f}$  is a vector valued function, and encapsulates the cell level electrophysiology. The variables  $\sigma_i$  and  $\sigma_o$  represent intracellular and extracellular conductivity tensors. It should be noted that the conductivity of cardiac tissue is anisotropic—it is not equally conductive in all directions, with higher conductivity along the fibre direction of the tissue.

Generally, no flux boundary conditions are applied to the domain:

$$\mathbf{n} \cdot (\sigma_i \nabla (V_m + \phi_o)) = 0 \quad \text{on } \partial\Omega, \quad (2.17)$$

$$\mathbf{n} \cdot (\sigma_o \nabla \phi_o) = 0 \quad \text{on } \partial\Omega, \quad (2.18)$$

where  $\mathbf{n}$  is the outward pointing normal vector to the computational domain.

It should be noted that the bidomain equations, as stated here, are degenerate—they

do not have a unique solution, specifying the value of  $\phi_o$  only up to an additive constant. However, as the parameter of interest is usually considered to be  $V_m$ , this does not affect the physiological usefulness of the equations.

Under certain regimes, it is possible to make a further assumption that the intra- and extra-cellular domains are equally anisotropic, differing only by a scaling factor  $k$ . By applying the approximation ( $\sigma_i = k\sigma_o$ ), the bidomain equations can then be simplified to produce the *monodomain equation*, which takes the form

$$\beta \left( C_m \frac{\partial V_m}{\partial t} + I_{\text{ion}}(\boldsymbol{\eta}, V_m) \right) - \nabla \cdot (\sigma_m \nabla V_m) = I_{\text{stim}} \quad \text{in } \Omega, \quad (2.19)$$

where  $\sigma_m = \sigma_i \sigma_o (\sigma_i + \sigma_o)^{-1}$  and represents the monodomain conductivity tensor, and  $I_{\text{stim}}$  represents the monodomain stimulus current.

It should be noted that the subsequent reduced complexity of computationally solving this equation compared to solving the coupled bidomain equations comes with a cost in terms of physiological accuracy. Generally, it may be considered that the monodomain is appropriate in cases where there is no significant anisotropy in the tissue e.g. interstitial spaces.

# Chapter 3

## Input Parameter Variation for a Computational Cell Model

The first work of this DPhil was to investigate the effect of parameter variation on the Mahajan model. This was for two purposes:

1. Investigate the stability of the model to small variations in input parameter values.
2. Investigate the possibility of a single parameter set being replaced by a *parameter space*. The corollary of this is that the model is *degenerate*, in that there are multiple different input parameter sets for the model that will provide an identical output.

To investigate the effects of parameter variation, a parameter sweep for the peak ion channel conductances for specific membrane channels for the Mahajan model is conducted. This has been conducted in two phases: the first was to perform a two-dimensional parameter sweep, varying the peak conductances for  $I_{Ks}$  and  $I_{CaL}$  ( $g_{Ks}$  and  $g_{CaL}$ , respectively); the results of this will be presented in §3.3. The second is to perform a more comprehensive six-dimensional parameter sweep, examining the model response to variation in the peak conductances for  $I_{Ks}$ ,  $I_{CaL}$ ,  $I_{K1}$ ,  $I_{Kr}$ ,  $I_{NaK}$ , and  $I_{to}$ . Methodology common to both phases is presented in §3.1.

### 3.1 Computational Methods

The Mahajan model was downloaded from the CellML repository, and intracellular  $K^+$  concentration ( $[K^+]_i$ ) was unclamped and allowed to vary according to

$$\frac{dK^+}{dt} = -\frac{\sum I_{Kx}A_{cap}}{FV_c}, \quad (3.1)$$

where  $\sum I_{Kx}$  represents the sum of all ion currents involving  $K^+$  movement across the membrane,  $A_{\text{cap}}$  represents the capacitive membrane area and  $V_c$  represents the volume of the compartment. The model was then run until steady state for the newly unclamped model were reached. The code was then converted by the COR program (Garny et al., 2003) to C++. A detailed parameter sweep is then conducted—every combination of the input parameters is used, producing  $n^m$  different results, where  $n$  is the number of values each parameter can take, and  $m$  is the number of parameters being varied.

For the 2-D sweep, the model was solved using a forward Euler method with a time-step of 0.005ms for a duration of 100 minutes. For the 6-D sweep, the simulation times was reduced to  $16\frac{2}{3}$  minutes (1,000,000ms) upon examination of COR output suggesting steady state was reached within 750,000ms, and the CVODE solver was implemented to allow for adaptive time-stepping.

Due to the non-spatial, non-stochastic nature of the model, the effect of reducing ion channel conductances can be considered to either reduce the peak conductance of each individual ion channel, or to reduce the number of ion channels in the cell as a whole. Parameters are varied based on a scaling from their ‘control’ values—the consequent values are shown in Table 3.1. For the 2-D sweep, a broad-range sweep over the parameter space  $[0.1, 5.0]$  was carried out, followed by a more in depth investigation of those scaling values closer to 1 ( $[0.5, 1.5]$ ). For the 6-D sweep, the parameter space for  $\pm 30\%$  at 15% intervals is searched.

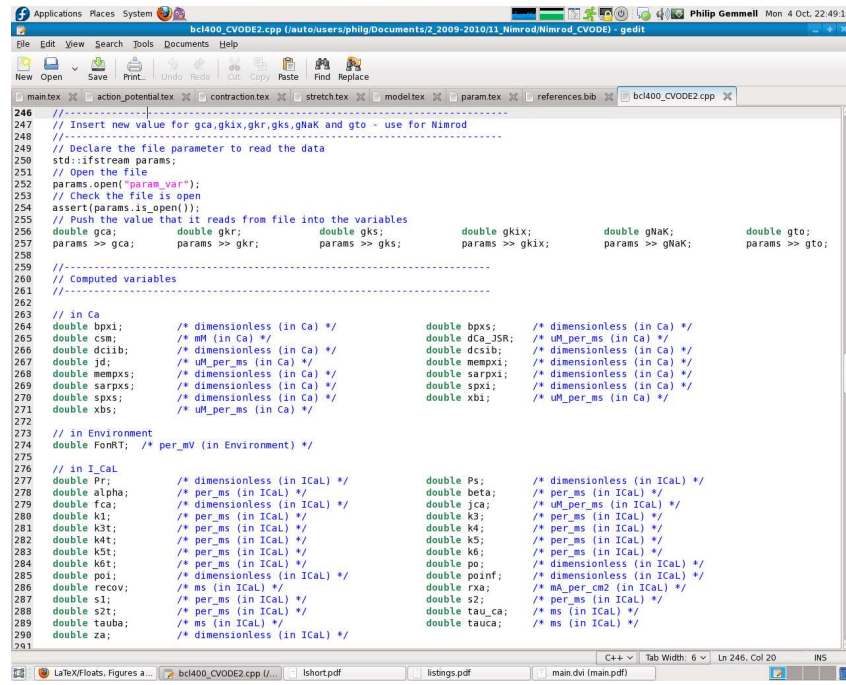
## The Nimrod/G Grid

To fully explore the 6-D parameter space, with each parameter taking one of 5 values, is a computationally expensive task—there are 15,625 permutations possible, and with each simulation taking approx. 5 minutes, this equates to more than 1,000 hours of CPU time required. Consequentially, performing this task on a single workstation is not feasible. To allow the required simulations to take place, the Nimrod/G grid computing system is taken advantage of (Abramson et al., 2000). Nimrod/G presents an architecture where an embarrassingly parallel program can, when coded correctly, be uploaded to the ‘root’ website, from which each job can be distributed to one of several nodes distributed globally. Consequently, the speed of the simulation is limited mainly by how many nodes are available—theoretically, the Nimrod/G grid makes it possible to run all 15,625 simulations simultaneously.

To use Nimrod/G to conduct a parameter sweep, an executable file must be generated that includes code that provides suitable instructions to the Nimrod software to instruct which parameters need to be varied. The code in this instance was written in C++, and the section of the program that codes for the insertion of new parameter values is shown in

Scale ( $g^{\text{scale}}$ )	$g_{\text{CaL}}$ (mmol/cmC)	$g_{\text{Ks}}$ (mS/ $\mu$ F)	$g_{\text{Kr}}$ (mS/ $\mu$ F)	$g_{\text{K1}}$ (mS/ $\mu$ F)	$g_{\text{NaK}}$ (mS/ $\mu$ F)
0.10	18.2	0.01386	—	—	—
0.50	91.0	0.06930	—	—	—
0.60	109.2	0.08316	—	—	—
0.70	127.4	0.09702	0.008750	0.210	1.050
0.75	136.5	0.10395	—	—	—
0.80	145.6	0.11088	—	—	—
0.85	154.7	0.11781	0.010625	0.255	1.275
0.90	163.8	0.12474	—	—	—
1.00	182.0	0.13860	0.012500	0.300	1.500
1.10	200.2	0.15246	—	—	—
1.15	209.3	0.15939	0.013475	0.345	1.725
1.20	218.4	0.16632	—	—	—
1.25	227.5	0.17325	—	—	—
1.30	236.6	0.18018	0.016250	0.390	1.950
1.40	254.8	0.19404	—	—	—
1.50	273.0	0.20790	—	—	—
2.50	455.0	0.34650	—	—	—
5.00	910.0	0.69300	—	—	—

**Table 3.1:** Range of parameter values used in 2-D and 6-D parameter sweeps. Where the value was not needed for the sweeps, a dash is included in the table. The parameter values for  $I_{to,f}$  and  $I_{to,s}$  are not included due to the method of scaling  $I_{to}$ , as explained in §2.4.2.



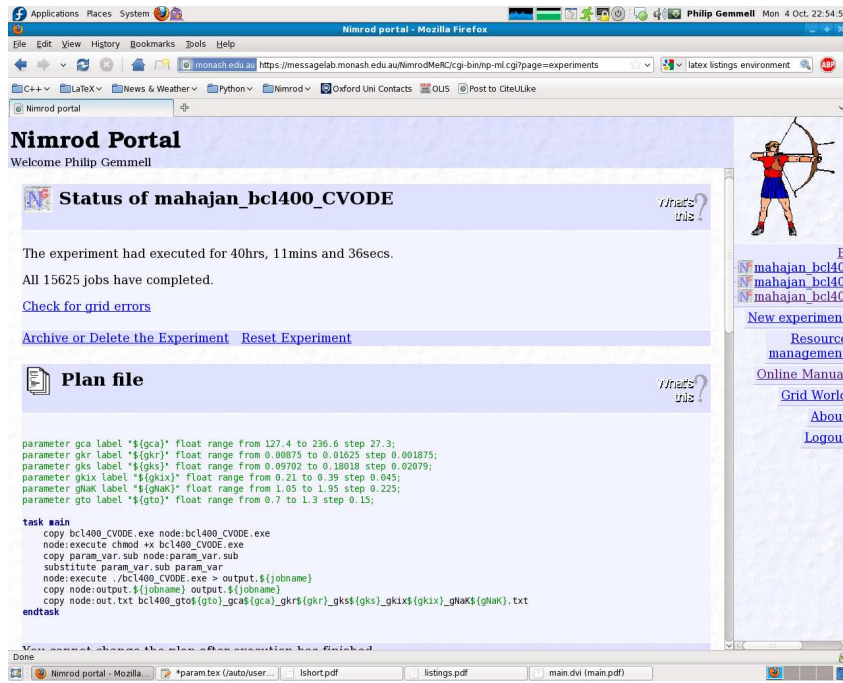
**Figure 3.1:** Example of a C++ file written to allow Nimrod to insert parameters for the variables *gca*, *gkr*, *gks*, *gkix*, *gnaK* and *gto*. The relevant section of code is shown at the top of the window—the file ‘param\_var.sub’ is opened, checked to be open, and then the values for the parameters are inserted into the code.

Fig. 3.1. This works in conjunction with a substitution file (in this case, ‘param\_var.sub’) and the Nimrod/G software to insert the values required into the program, before this program is run on one of the nodes in the grid.

The other component in the Nimrod/G architecture is the plan file—an example is shown in Fig. 3.2. The initial part of the plan file instructs Nimrod what parameters are to be searched over—this can either be done as here, with a discrete stepping approach, or individual values to investigate can be inputted. The next part is the ‘main task’, which details how Nimrod is to search over these values. It instructs Nimrod to copy the executable from the website, where it has been uploaded by the user, to the ‘node’, where it can be executed. The parameter substitution file is also copied across, and then the substitution is performed in the program. This program is then executed, and the resulting output copied to a text file.

## 3.2 Analysis of Results

Once the simulation has been run, the last two APs of the simulation are compared against each other with a least square difference method, both for membrane potential ( $V_m$ ) and cytosolic  $\text{Ca}^{2+}$  concentration ( $[\text{Ca}^{2+}]_i$ ), to ensure steady state has been reached.



**Figure 3.2:** Example of the Nimrod/G root website, displaying the plan file the the 6-D parameter sweep.

If the simulation is not at steady state, no further analysis is performed. If steady state is reached, the values for AP duration (APD) are calculated, for 90%, 50% and 30% repolarisation; APD is considered as the interval between  $\frac{dV_m}{dt}$  reaching its maximum value during the upstroke, and the membrane potential repolarising by the specified percentage. Furthermore, the shape of the AP and the  $\text{Ca}^{2+}$  transient are compared to the control (where the ‘control’ is considered to be the output of the Mahajan model with no scaling applied to the parameter values) by summing the absolute difference between each recorded data value; data are recorded at intervals of 0.1ms. The calculation of both APD and absolute difference allows it to be established whether or not APD can be considered a reliable indicator of fit, or if the more rigorous (and more computationally intensive) absolute difference calculation is required to accurately assess goodness of fit.

The above methodology is suitable for both the 2-D and 6-D parameter sweeps; however, the task of efficiently and coherently representing the data from the 6-D parameter sweep requires a further stage of analysis. Consequently, the data from the 6-D parameter sweep will be sorted using the technique of clutter-based dimension reordering (CBDR). This is a method of representing a multi-dimensional parameter space as a two-dimensional image through linear projection (Peng et al., 2004; Taylor et al., 2006). It is then possible to refine the method of this linear projection to allow identification of those parameters that have the greatest effect on the output.

The first stage in the CBDR method is to set all parameters apart from two (chosen at

random) to their minimum possible value, and then plot the effect of the two remaining parameters on the output metric. How this output metric is measured is variable: in Taylor et al. (2006), the continuous output metric is split into discrete categories, but for this paper we use a continuous contour-based measurement i.e. the first stage of this method here produces a contour plot of the output (e.g.  $APD_{90}$ ). The next step is to select two other parameters, and replot the initial 2-D plot for each of these parameters. The resulting collection of plots is arranged in a 2-D pattern, e.g. for measuring 4 parameters, each with 5 values, the resulting plot would be a  $(5 \times 5) \times (5 \times 5)$  plot, that is, a  $(25 \times 25)$  plot. This plotting arrangement is repeated until all parameters have been plotted. An example of this plotting technique, referred to as dimensional stacking, is shown in Fig. 3.3.

The next stage of this methodology involves defining a scoring metric for the stacked grid. In the case of the 6-D image to be considered in this thesis, this involves calculating the root mean square (RMS) difference between each point on the final grid and its ‘neighbours’. There are two definitions of neighbour in common usage for a square grid: the first is more restrictive, and defines a neighbour to be a point on the grid that differs by one grid step in one dimension from the original point, thus giving each point (apart from edge points) four neighbours. The second defines a neighbour to be one grid step apart in multiple dimensions, giving eight neighbours for each point (again, save edge points). The more restrictive definition will be used, like in Taylor et al. (2006), who established that, even with this more restrictive definition, different behaviour types were still highly connected (recall Taylor et al. (2006) used discretised data instead of continuous data. It is not expected that this difference will affect the conclusions).

Once this score has been calculated, it is compared to the score for ‘neighbours’ of this grid configuration. In this context, a neighbour is a grid configuration that differs only by swapping two of the dimensions in the stack order. Consequently, each grid configuration has  $n(n-1)$  neighbours, where  $n$  is the number of dimensions being stacked. If a neighbour has a lower RMS score, that stack order is chosen, and the scoring process for it and its neighbours is repeated. The iterative process works to minimise the RMS score—once a stack order has the lowest score of itself and its neighbours, a minimum is said to have been reached. This process needs to be repeated several times, with a different start order for the dimensional stacking each time, to ensure a global minimum has been reached, and not just a local minimum.

The purpose of finding this global minimum is that it helps to elucidate which parameters are most influential to the output metric by grouping ‘islands’ of certain behaviour types together. An example of this process, and its success, is shown in Fig. 3.4. With this CBDR method, it is hoped to be able to find patterns within the 6-D parameter



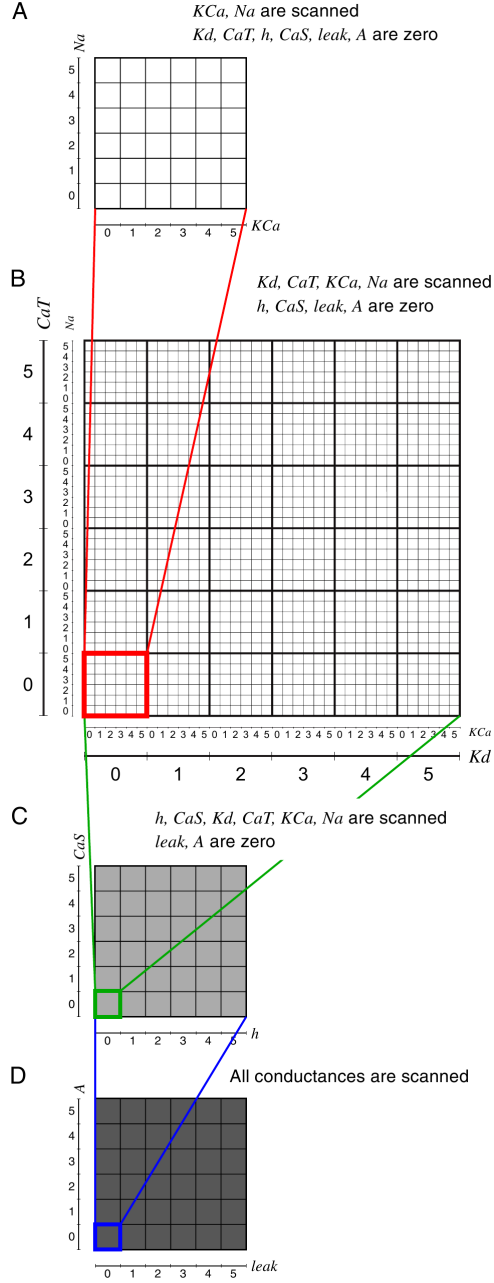


**Figure 3.3:** Example of dimensional stacking, for parameters varied in Taylor et al. (2006). (A) Visualisation of two conductances ( $\bar{g}_{KCa}$  and  $\bar{g}_{Na}$ ) with all other conductances set to their minimum value. (B) The grid from (A) is embedded in a larger grid, which scans an additional two conductances ( $\bar{g}_{Kd}$  and  $\bar{g}_{CaT}$ ). The original grid from (A) is at the bottom left corner, as it corresponds to the minimum conductance values for the two new parameters. This process is repeated in (C) and (D) to give the final 2-D representation of a 8-D parameter space. Source: Taylor et al. (2006)

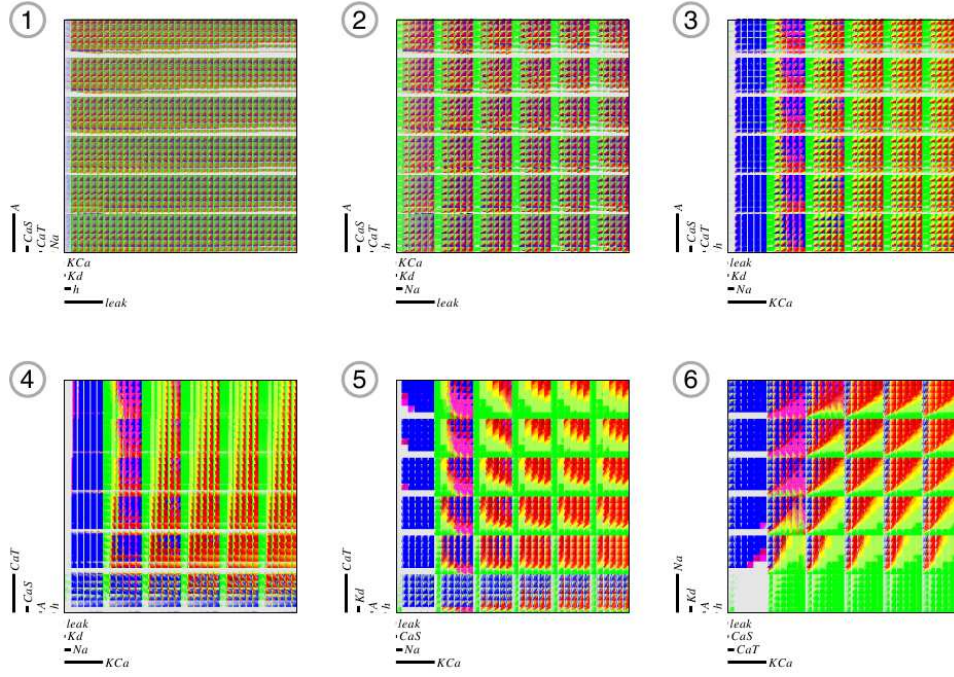


**Figure 3.4:** Example of the implementation of clutter-based dimension reordering, using the data from Prinz et al. (2003). In this instance, the data were split into discrete categories, and the scoring system aimed to minimise the number of different coloured blocks in the image. The initial dimension stacking order is shown in (1), with subsequent re-orderings shown up to the final dimension stack order in (6).

Source: Taylor et al. (2006)

sweep, and isolate which of the various membrane currents varied have the greatest effect on the repolarisation mechanisms of the cell model.

### 3.3 2-D Parameter Sweep Results and Discussion

Fig. 3.5 shows the results for APD, AP shape and  $\text{Ca}^{2+}$  transient shape differences from control to different parameter scaling values for  $g_{\text{CaL}}^{\text{scale}} = [0.1, 2.5]$  and  $g_{\text{Ks}}^{\text{scale}} = [0.1, 5.0]$ . They demonstrate that linear changes in the input parameter set do not lead to linear changes in the output—the precise structure of the output landscape is a complex matter, with the greatest differences in output not necessarily correlating to the greatest differences in input. This can be seen in Fig. 3.5(F), which shows the similarity between the control AP and the AP produced when  $g_{\text{CaL}}$  and  $g_{\text{Ks}}$  are both scaled to five times their original value. It can be noted, however, that the plateau is noticeably shortened, implying  $I_{\text{Ks}}$  (which shortens the AP when increased) plays a greater role in AP shape determination than  $I_{\text{CaL}}$  (which lengthens the AP when increased). The results also indicate some robustness to small parameter variation, and furthermore that the impact

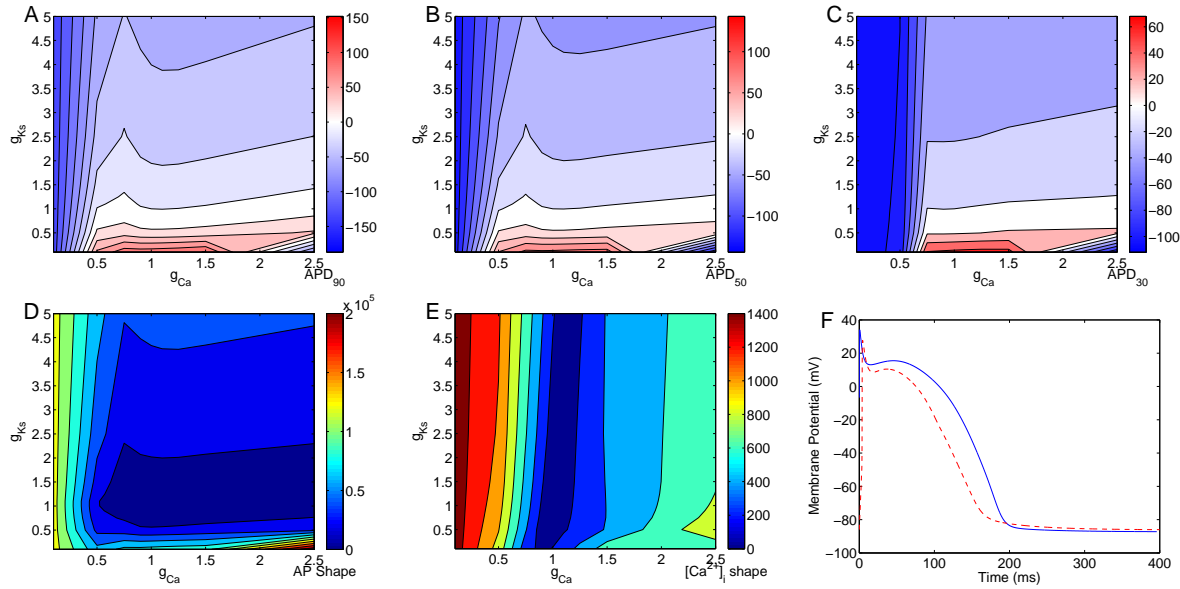


**Figure 3.5:** Effects of varying  $g_{CaL}$  and  $g_{Ks}$ . (A)-(C) are contour plots displaying the difference between the control APD and the APD for the model with  $g_{CaL}$  and  $g_{Ks}$  scaled as indicated in the axes, for  $APD_{90}$ ,  $APD_{50}$  and  $APD_{30}$  respectively. (D) shows the summed absolute difference between control and simulation for the AP shape, and (E) the same for the  $Ca^{2+}$  transient. (F) plots the AP for the control input parameter values (solid line) and for the scaling by 5.0 (dashed line). Since steady state was not reached for some simulations with  $g_{CaL}^{scale} = 5$ , results for  $g_{CaL}^{scale} = 5$  have been excluded from the contour plots—the next available data for  $g_{CaL}$  are  $g_{CaL}^{scale} = 2.5$ .

on output by large variations in one parameter can be mitigated by large variations in another.

Fig. 3.6 shows the results for  $\pm 50\%$  parameter variation. It includes a plot of the control AP (Fig. 3.6(F)), and the AP for  $g_{CaL}^{scale} = 0.5$ ,  $g_{Ks}^{scale} = 0.7$ . Comparison with Fig. 3.5(F) demonstrates that, in this instance, a smaller scaling of input parameters leads to a greater difference in the output—this is due mainly to the parameter set leading to a reduced ‘plateau’ potential, coupled with a more rapid repolarisation.

Steady state is not reached for the parameter set  $g_{CaL}^{scale} = 5.0$ ,  $g_{Ks}^{scale} = \{0.5, 0.75, 0.9, 1.0, 1.1, 1.5\}$ —however, a stable form of alternans is reached (data not shown). The common thread to these parameter values is the high scaling of  $g_{CaL}$  compared to  $g_{Ks}$ , thus implying the increased  $I_{CaL}$  is responsible for the observed alternans. Assuming increased  $I_{CaL}$  will lead to increased  $Ca^{2+}$  flux in the cell, this will in turn lead to increased interval  $[Ca^{2+}]_i$ . It is likely that this is the root cause for CTA, which in turn leads to  $V_m$  alternans, as opposed to  $V_m$  alternans causing  $Ca^{2+}$  alternans—the increase in  $I_{CaL}$  presents a means for  $Ca^{2+}$  alternans to be induced through pathological  $Ca^{2+}$  variation, while no mechanism for AP alternans is readily apparent. Further investigations will have to be conducted to verify this hypothesis in this instance. These results imply that an increased

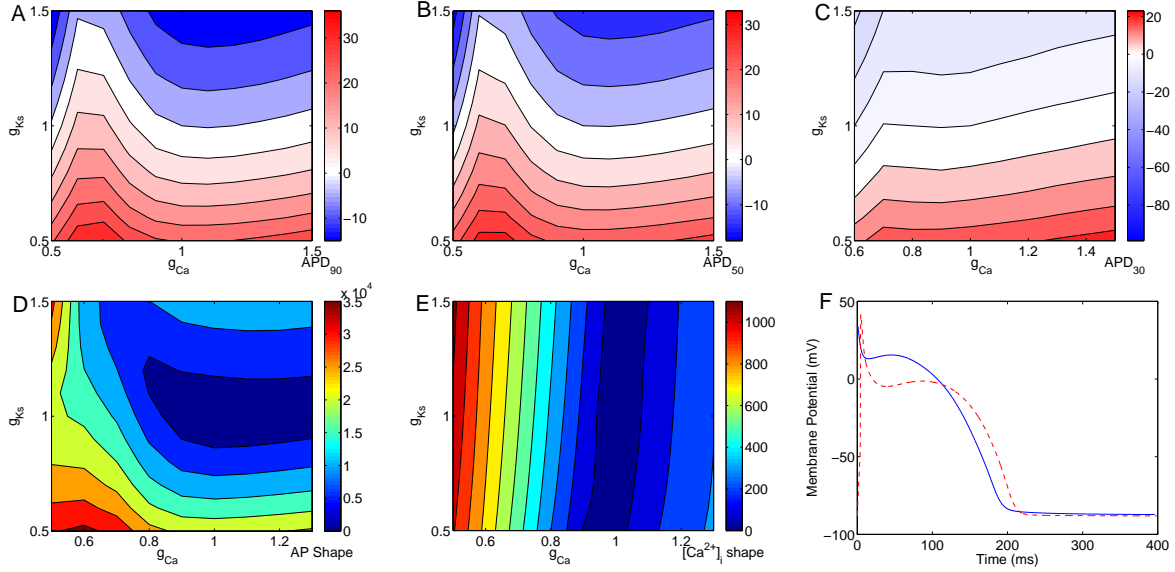


**Figure 3.6:** Effects of varying  $g_{CaL}$  and  $g_{Ks}$  near the control value. (A)–(C) are contour plots displaying the difference between the control APD and the APD for the model with  $g_{CaL}$  and  $g_{Ks}$  scaled as indicated in the axes, for APD<sub>90</sub>, APD<sub>50</sub> and APD<sub>30</sub> respectively. (D) shows the summed absolute difference between control and simulation for the AP shape, and (E) the same for the  $Ca^{2+}$  transient. The parameter range shown in (C) is smaller than in the other plots—the reason for this is demonstrated in (F), which plots the AP for the control input parameter values (solid line) and for  $g_{CaL}^{scale} = 0.5, g_{Ks}^{scale} = 0.7$ . The rapid initial repolarisation leads to values for APD<sub>30</sub> that are far smaller than for any other simulation result. Consequently, the contour levels in (C) would be dominated by displaying those values.

$Ca^{2+}$  transient mechanism (e.g. increased  $g_{CaL}$ ) with no off-setting mechanism in place (e.g. increased  $I_{Ks}$ ) has a profound impact on the AP.

It is worth noting that  $g_{CaL}^{scale} = 5.0, g_{Ks}^{scale} = 1.25$  produced a steady state output (data not shown)—this ‘island’ of stability in the range noted above serves to emphasise the non-linear, non-trivial nature of the interactions between currents.

The results also show significant differences between the results for APD difference and for the AP shape absolute difference. All APD data demonstrated similar results, but the contour plot for AP shape is markedly different. These results suggest that APD is not sufficient to fully assess the similarity between two different AP traces. It is also worth noting the different landscape for AP shape and  $Ca^{2+}$  transient shape, demonstrating their different reactions to input parameter variation. This indicates that a model may provide a very good fit by one metric, and yet may be entirely inaccurate when measured against a different metric.

Comparing the landscapes for all five contour plots, it is by no means certain that degeneracy for input parameter values exist—the results suggest a ‘trough’ in the landscape for APD, thus suggesting a degeneracy, but this trough does not appear to coincide with

another trough for AP and  $\text{Ca}^{2+}$  shape, and thus, for the parameter space examined, the model does not exhibit degeneracy.



# Chapter 4

## Future Work

It is proposed to use the remaining portion of this DPhil to investigate the following questions:

1. Does the inclusion of heterogeneity in ion channel properties explain the cell-to-cell variation observed in tissue?
2. Can the inclusion of heterogeneity, ECC and MEF in a tissue model explain the development of ventricular fibrillation (VF) and other repolarisation phenomena in response to tachycardia?

### 4.1 Cell-to-Cell Variability

As has been stated, in experimental recordings there exists a cell-to-cell variability between cells taken from the same tissue. This variability can be reproduced using a phenomenological model (Walmsley et al., 2010), but by its nature this model does not investigate the physiological reasons behind the variability. As such, the next stage proposed in this research will be to investigate whether the cell-to-cell variation demonstrated experimentally can be captured *in silico* by implementation of parameter variation in the cardiac ion channels.

The investigation of these effects will be an extension of the 6-D parameter sweep conducted for the Mahajan model. In that work, the parameter set was replaced with a parameter space of possible sets, all of which gave the same AP result. This work served to confirm the viability of changing the parameter set of a model to a parameter sapce with little impact on the output the cell model.

Using the results from the 6-D parameter sweep, a similar parameter sweep will be conducted for the Restrepo/Chen model, this time incorporating the possibility of variation in the CSQN buffering of the RyR channels, and also of the coupling between RyR

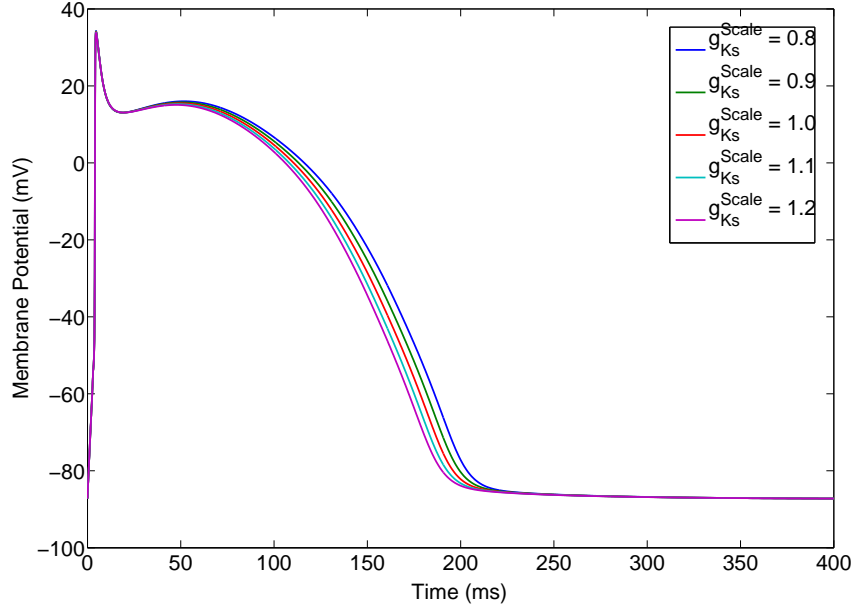


**Figure 4.1:** *Plot demonstrating the effect of varying  $g_{Ks}$  on AP. With all other parameter values held at their ‘control’ values given in the Mahajan paper,  $g_{Ks}$  is varied to demonstrate the impact on the AP, and specifically on the repolarisation effects.*

channels. With this sweep, direct comparison to experimental evidence can be made to assess whether the experimental cell-to-cell variability is captured by variation within the parameter space. The difference between the assessment of the Mahajan sweep and this proposed sweep should be noted: the former is a computational assessment, comparing the results to the ‘control’ simulation output, whereas the latter will be assessed in comparison to experimental data.

The Mahajan sweep has already demonstrated the validity of this proposed investigation—Fig. 4.1 demonstrates how the variation in just one parameter ( $g_{Ks}$ ) can have a profound effect on the AP. Consequently, a fully-realised 6-D parameter sweep for the Chen/Restrepo model is expected to provide a detailed, realistic space in which parameter values can lie and still produce a physiological output at normal pacing rates.

## 4.2 Tissue-level Effects of Heterogeneity and Stretch

The hypothesis being proposed is that the small variations in the parameter sets that are postulated to exist between cells, that present no discernable impact on the AP at normal pacing rates, can present a method for a dangerous heterogeneity in the tissue to be introduced when the simulation is run at high pacing rates. This investigation will be conducted in a multi-scale simulation framework, with account taken for both ECC and



MEF to provide a biologically realistic simulation setting in which to test the hypothesis. The multi-scale simulation will allow closer examination of the multi-scale mechanisms that lead to VF. The three scales of interest are the subcellular, the cellular and the tissue—each of these regimes presents a new emergent property, which depends to some degree on the preceding scale.

The hypothesis proceeds thus: at the subcellular level, the stochastic nature of the CRUs and the  $\text{Ca}^{2+}$  spark process can have a demonstrable effect on the  $\text{Ca}^{2+}$  transient, and consequently on the AP waveform. The stochastic nature of this means there is a nonuniform aspect to  $\text{Ca}^{2+}$  release across the cell—the cell cannot be thought of, using this model, as a ‘black box’ providing constant output to constant input. The AP waveform can, in turn, be drastically affected by the properties of the ion channels affecting ion flow in and out of the cell (the modified AP will then in turn affect the ion flow in a feedback process). With the modifications made in the previous section, not all cells in a tissue simulation are the same—there is now a level of heterogeneity at both the subcellular and cellular level.

The heart can undergo several different stresses and strains during its operation. For example, the ventricles could over-fill during diastole, causing strain to be placed on the ventricular tissue. Alternatively, heart rate could increase due to the exertions of exercise—there are a number of possible scenarios that can perturb the normal, physiological running of the heart. However, as a consequence of these pathologies, heterogeneities between the cells in the tissue are exacerbated. At normal pacing rates, by design this heterogeneity is benign. However, as the pacing rate is increased, it is hypothesised that these differences become malign—the increased pacing rate will lead to individual cells in the simulation exhibiting different  $\text{Ca}^{2+}$  transients and AP waveforms, with different repolarisation dynamics, and consequently different refractory periods which, at a tissue level, could prove dangerous. These heterogeneities in the repolarisation mechanisms and  $\text{Ca}^{2+}$  dynamics could provide the seed for reentrant waves, EADs and DADs.

This research aims to investigate the effect of pathological conditions on a physiologically realistic tissue model. The pathologies to be investigated will include, but will not necessarily be limited to, the effects of stretch and  $\text{Ca}^{2+}$  overload on the cell. These pathologies are known to have effects on the function of cardiac tissue—for example, the inactivation of LCC, modulating  $I_{\text{CaL}}$ , is known to be affected by  $[\text{Ca}^{2+}]_i$ , and thus  $\text{Ca}^{2+}$  overload can have a noticeable impact. The hypothesis under investigation is that the combination of MEF, ECC, physiological parameter variation and other known environmental factors will reveal dangerous heterogeneities on the macroscopic scale in cardiac tissue.

It is the goal of this DPhil to implement these sources of heterogeneities in a real-

istic multi-scale model, then use this model to investigate the subcellular and cellular mechanisms responsible for these tissue-level phenomena.

### 4.3 Construction of a Multi-Scale Model

A major portion of this DPhil will be used in the construction of an accurate multi-scale model, but this model will not be constructed from scratch—it will make use of several earlier pieces of work, with the major novel aspect being in the combination of the different sections.

The cell model to be used will be the modified Chen/Restrepo model (hereafter referred to as the mCR model) resulting from the work conducted in the previous section—this will provide heterogeneity in the parameter sets. The nature of the mCR model allows investigation of the subcellular regime, by means of the CRUs. As demonstrated in Chen et al. (2009), and discussed in §2.4, the subcellular mechanisms of  $\text{Ca}^{2+}$  sparks has a demonstrable effect on the cellular level—the paper demonstrates a link between the  $\text{Ca}^{2+}$  spark dynamics and the introduction of DADs in the cell. Consequently, the mCR model is the perfect choice to allow a full understanding of the multi-scale mechanisms at work, and to assess the interactions between subcellular  $\text{Ca}^{2+}$  sparks, the cellular AP waveform, and the tissue ventricular AP wave dynamics.

It is intended to adapt the mCR model to include terms for ECC and MEF. ECC is the more studied of the two phenomena, and will be included to allow complete modelling of the ionic processes—the contraction of a cell will lead to a subsequent decrease in cellular volume, which will in turn lead to an increase in ionic concentrations. MEF is a less well-studied phenomenon, and consequently, a biomechanical mechanism for known effects cannot be expected to be located in all cases. Thus, while some effects will be modelled directly, such as SACs, many stretch effects, such as the acute effects of axial stretch (Iribe et al., 2009) will be reproduced on a phenomenological basis.

The next required stage is to embed the resulting mCR model in a tissue framework. This framework will be provided by embedding the model in the Cancer, Heart and Soft Tissue Environment (CHASTE). CHASTE is a general purpose simulation package aimed at multi-scale, computationally demanding problems arising in biology, but provides the opportunity to embed a cell model in a tissue simulation (Pitt-Francis et al., 2009). Once the mCR model is thus embedded, the simulation will be adapted to provide each cell in the tissue simulation with a different parameter set. This will finally provide a complete, multi-scale tissue model that includes mechanisms for subcellular stochasticity, parameter variation, ECC and MEF, that can be used to test the hypothesis.

It should be noted that the construction of the above model is not a trivial matter.

The proposed model, with calculations ranging on the spatial scale from sub-cellular to tissue, is a novel attempt to investigate the subcellular causes of tissue-level phenomena. Consequently the model will require a great deal of programming effort, with the end result likely being a computationally intensive simulation—great efforts will have to be made to ensure that the model is both realistic and also computationally tractable.

## 4.4 Proposed Timeline for Research

It is proposed to conduct the research suggested in this Future Work section according to the following timeline. It should be noted that this timeline remains pliable, and does not reflect a strict schedule—it will adapt as problems prove simpler or more difficult to accommodate the time required.

<b>October 2010</b>	Conduct literature review of EADs, DADs and VF.
<b>November 2010</b>	Conduct analysis of results of 6-D parameter sweep. Investigate for signs of model degeneracy, and possibility of replacing a computer model's parameter set with a parameter space without changing the output results
<b>November 2010</b>	Conduct literature review into modelling techniques for ECC.
<b>December 2010</b>	Implement Chen model. Revise to include CSQN buffering, and investigate how to implement in Nimrod/G.
<b>January 2011</b>	Include ECC in Chen model.
<b>March 2011</b>	Conduct literature review into modelling of MEF, including modelling of SACs.
<b>May 2011</b>	Implement MEF into mCR model.
<b>July 2011</b>	Conduct literature review into tissue modelling techniques.
<b>August 2011</b>	Implement the mCR model into the CHASTE framework for tissue simulation.
<b>October 2011</b>	Determine which parameters to vary in mCR tissue (mCRt) model, then conduct multi-dimensional parameter sweep of the mCR model.
<b>November 2011</b>	Compare results of mCRt parameter sweep to experimental data. Use results to determine valid parameter space.
<b>January 2012</b>	Begin conducting experiments with heterogeneous mCRt (hmCRt) model at high pacing rates.
<b>March 2012</b>	Conduct experiments using the hmCRt model to investigate other pathological regimes e.g. stretch, $\text{Ca}^{2+}$ overload.
<b>June 2012</b>	Start writing up results, both for DPhil thesis and other relevant papers.
<b>October 2012</b>	Hand in completed DPhil thesis.

It should be noted that, throughout this timeline, when interesting results are given

by an experiment, it will be aimed to write those results up for publication.

# Bibliography

- Abramson, D., Giddy, J., and Kotler, L. (2000). High performance parametric modeling with Nimrod/G: Killer application for the global grid? In *International Parallel and Distributed Processing Symposium (IPDPS)*.
- Bassani, J. W. M., Yuan, W., and Bers, D. M. (1995). Fractional SR Ca release is regulated by trigger Ca and SR Ca content in cardiac myocytes. *American Journal of Physiology: Cell Physiology*, 268:C1313–C1319.
- Bassani, R. A., Altamirano, J., Puglisi, J. L., and Bers, D. M. (2004). Action potential duration determines sarcoplasmic reticulum  $\text{Ca}^{2+}$  reloading in mammalian ventricular myocytes. *Journal of Physiology*, 559:593–609.
- Belus, A. and White, E. (2003). Streptomycin and intracellular calcium modulate the response of single guinea-pig ventricular myocytes to axial stretch. *Journal of Physiology*, 546:501–509.
- Bers, D. M. (2001). *Excitation contraction coupling and cardiac contractile force*, 2nd Ed. Kluwer Academic Publishers, Boston.
- Calaghan, S. C. and White, E. (1999). The role of calcium in the response of cardiac muscle to stretch. *Progress in Biophysics & Molecular Biology*, 71:59–90.
- Carmeliet, E. and Vereecke, J. (2002). *Cardiac Cellular Electrophysiology*. Kluwer Academic Publishers.
- Chen, W., Wasserstrom, J. A., and Sherifaw, Y. (2009). Role of coupled gating between cardiac ryanodine receptors in the genesis of triggered arrhythmias. *American Journal of Physiology—Heart and Circulatory Physiology*, 297:H171–H180.
- Chen-Izu, Y., McCulle, S. L., Ward, C. W., Soeller, C., Allen, B. M., Rabang, C., Cannell, M. B., Balke, C., and Izu, L. T. (2006). Three-dimensional distribution of ryanodine receptor clusters in cardiac myocytes. *Biophysical Journal*, 91:1–13.

- Chudin, E., Goldhaber, J., Garfinkel, A., Weiss, J., and Kogan, B. (1999). Intracellular  $\text{Ca}^{2+}$  dynamics and the stability of ventricular tachycardia. *Biophysical Journal*, 77:2930–2941.
- Cleeman, L., Wang, W., and Morad, M. (1998). Two-dimensional confocal images of organization, density and gating of focal  $\text{Ca}^{2+}$  release sites in rat cardiac myocytes. *Proceedings of the National Academy of Sciences*, 95:10984–10989.
- Cooper, G. M. (2000). *The Cell: A molecular approach*. Sinauer Associates, second edition.
- Franzini-Armstrong, C., Protasi, F., and Ramesh, V. (1999). Shape, size and distribution of  $\text{Ca}^{2+}$  release units and couplons in skeletal and cardiac muscles. *Biophysical Journal*, 77:1528–1539.
- Garny, A., Kohl, P., and Noble, D. (2003). Cellular Open Resource (COR): a public CellML based environment for modelling biological function. *Int. J. Bif. Chaos*, 13:3579–3590.
- Greenstein, J. L. and Winslow, R. L. (2002). An integrative model of the cardiac ventricular myocyte incorporating local control of  $\text{Ca}^{2+}$  release. *Biophysical Journal*, 83:2918–2945.
- Gurev, V., Maleckar, M. M., and Trayanova, N. A. (2006). Cardiac defibrillation and the role of mechanoelectric feedback in postshock arrhythmogenesis. *Annals of the New York Academy of Sciences*, 1080:320–333.
- Hodgkin, A. L. and Huxley, A. F. (1952). A quantitative description of membrane current and its application to conduction and excitation in nerve. *Journal of Physiology*, 117:500–544.
- Hutter, O. F. and Noble, D. (1960). Rectifying properties of heart muscle. *Nature*, 188:495.
- Inoue, R., Jensen, L. J., Shi, J., Morita, H., Nishida, M., Honda, A., and Ito, Y. (2006). Transient receptor potential channels in cardiovascular function and disease. *Circulation Research*, 99:119–131.
- Iribe, G. and Kohl, P. (2008). Axial stretch enhances sarcoplasmic reticulum  $\text{Ca}^{2+}$  leak and cellular  $\text{Ca}^{2+}$  reuptake in guinea pig ventricular myocytes: Experiments and models. *Progress in Biophysics & Molecular Biology*, 97:298–311.

- Iribe, G., Ward, C. W., Camelliti, P., Bollensdorff, C., Mason, F., Burton, R. A. B., Garry, A., Morphew, M. K., Andreas Hoenger, W. J. L., and Kohl, P. (2009). Axial stretch of rat single ventricular cardiomyocytes causes an acute and transient increase in  $\text{Ca}^{2+}$ spark rate. *Circulation Research*, 104:787–795.
- Isenberg, G., Kazanski, V., Kondratev, D., Gallitelli, M. F., Kiseleva, I., and Kamkin, A. (2003). Differential effects of stretch and compression on membrane currents and  $[\text{Na}^+]_c$  in ventricular myocytes. *Progress in Biophysics & Molecular Biology*, 82:43–56.
- Jurkat-Rott, K. and Lehmann-Horn, F. (2005). Muscle channelopathies and critical points in functional and genetic studies. *Journal of Clinical Investigation*, 115:2000–2009.
- Kamisago, M., Sharma, S. D., DePalma, S. R., Solomon, S., Sharma, P., McDonough, B., Smoot, L., Mullen, M. P., Woolf, P. K., Wigle, D., Seidman, J. G., and Seidman, C. E. (2000). Mutations in sarcomere protein genes as a cause of dilated cardiomyopathy. *New England Journal of Medicine*, 343:1688–1696.
- Keener, J. and Sneyd, J. (1998). *Mathematical Physiology*. Springer.
- Kohl, P., Sachs, F., and Franz, M. R. (2005). Cardiac mechano-electric feedback: from pipette to patient. In Kohl, P., Sachs, F., and Franz, M. R., editors, *Cardiac Mechano-Electric Feedback and Arrhythmias*, pages xi–xiii. Elsevier Saunders.
- Kupittayanant, P., Trafford, A. W., Díaz, M. E., and Eisner, D. A. (2006). A mechanism distinct from the l-type  $\text{Ca}^{2+}$  current or  $\text{Na}^+$ - $\text{Ca}^{2+}$  exchange contributes to  $\text{Ca}^{2+}$  entry in rat ventricular myocytes. *Cell Calcium*, 39:417–423.
- Luo, C. H. and Rudy, Y. (1991). A model of the ventricular cardiac action potential. Depolarization, repolarization and their interaction. *Circulation Research*, 68:1501–1526.
- Luo, C. H. and Rudy, Y. (1994a). A dynamic model of the cardiac ventricular action potential. I. Simulations of ionic currents and concentration changes. *Circulation Research*, 74:1071–1096.
- Luo, C.-H. and Rudy, Y. (1994b). A dynamic model of the cardiac ventricular action potential. II. Afterdepolarizations, triggered activity and potentiation. *Circulation Research*, 74:1097–1113.
- Mahajan, A., Shiferaw, Y., Sato, D., Baher, A., Olcese, R., Xie, L.-H., Yang, M.-J., Chen, P.-S., Restrepo, J. G., Karma, A., Garfinkel, A., Qu, Z., and Weiss, J. N. (2008). A

- rabbit ventricular action potential model replicating cardiac dynamics at rapid heart rates. *Biophysical Journal*, 94:392–410.
- Matsuda, N., Hagiwara, N., Shoda, M., Kasanuki, H., and Hosoda, S. (2008). Enhancement of the L-type  $\text{Ca}^{2+}$  current by mechanical stimulation in single rabbit cardiac myocytes. *Biophysical Journal*, 94:392–410.
- Morris, C. E. and Laitko, U. (2005). The mechanosensitivity of voltage-gated channels may contribute to cardiac mechano-electric feedback. In Kohl, P., Sachs, F., and Franz, M. R., editors, *Cardiac Mechano-Electric Feedback and Arrhythmias*, pages 33–41. Elsevier Saunders.
- Noble, D. (1960). Cardiac action and pacemaker potentials based on the Hodgkin-Huxley equations. *Nature*, 188:495–497.
- Peng, W., Ward, M. O., and Rundensteiner, E. A. (2004). Clutter reduction in multi-dimensional data visualization using dimension reordering. In *Proceedings of the IEEE Symposium on Information Visualization 2004*.
- Petroff, M. G. V., Kim, S. H., Pepe, S., Dessy, C., Marbán, E., Balligand, J.-L., and Soltoff, S. J. (2008). Endogenous nitric oxide mechanisms mediate the stretch dependence of  $\text{Ca}^{2+}$  release in cardiomyocytes. *Nature Cell Biology*, 95:3767–3789.
- Picht, E., DeSantiago, J., Blatter, L. A., and Bers, D. M. (2006). Cardiac alternans do not rely on diastolic sarcoplasmic reticulum calcium content fluctuations. *Circulation Research*, 99:740–748.
- Pitt-Francis, J., Pathmanathan, P., Bernabeu, M. O., Bordas, R., Cooper, J., Fletcher, A. G., Mirams, G. R., Murray, P., Osborne, J. M., Walter, A., Chapman, S. J., Garny, A., van Leeuwen, I. M. M., Maini, P. K., Rodriguez, B., Waters, S. L., Whiteley, J. P., Byrne, H. M., and Gavaghan, D. J. (2009). Chaste: a test-driven approach to software development for biological modelling. *Computer Physics Communications*, 180:2452–2471.
- Prinz, A. A., Billimoria, C. P., and Marder, E. (2003). Alternative to hand-tuning conductance-based models: construction and analysis of databases of model neurons. *Journal of Neurophysiology*, 90:3998–4015.
- Puglisi, J. L. and Bers, D. M. (2001). LabHEART: an interactive computer model of rabbit ventricular myocyte ion channels and Ca transport. *American Journal of Physiology: Cell Physiology*, 281:2049–2060.



- Restrepo, J. G., Weiss, J. N., and Karma, A. (2001). Calsequestrin-mediated mechanism for cellular calcium transient alternans. *Biophysical Journal*, 3:867–873.
- Roden, D. M., Balser, J. R., Jr., A. L. G., and Anderson, M. E. (2002). Cardiac ion channels. *Annual Review of Physiology*, 64:431–475.
- Romero, L., Carbonell, B., Trenor, B., Rodriguez, B., Saiz, J., and Ferrero, J. M. (2010). Human and rabbit inter-species comparison of ionic mechanisms of arrhythmic risk: a simulation study. In *Proceedings of the 32nd Annual International IEEE EMBS Conference 2010*.
- Rudy, Y. and Silva, J. R. (2006). Computational biology in the study of cardiac ion channels and cell electrophysiology. *Quarterly Reviews of Biophysics*, 39:57–116.
- Sachs, F., Sigurdson, W., Ruknudin, A., and Bowman, C. (1991). Single-channel mechanosensitive currents. *Science*, 253:800–801.
- Shannon, T. R., Wang, F., Puglisi, J., Weber, C., and Bers, D. M. (2004). A mathematical treatment of integrated Ca dynamics within the ventricular myocyte. *Biophysical Journal*, 87:3351–3371.
- Sherifaw, Y., Watanabe, M. A., Garfinkel, A., Weiss, J. N., and Karma, A. (2003). Model of intracellular calcium cycling in ventricular myocytes. *Biophysical Journal*, 85:3666–3686.
- Stern, M. D. (1992). Theory of excitation-contraction coupling in cardiac muscle. *Biophysical Journal*, 63:497–517.
- Taylor, A. L., Hickey, T. J., Prinz, A. A., and Marder, E. (2006). Structure and visualization of high-dimensional conductance spaces. *Journal of Neurophysiology*, 258:891–905.
- Tohse, N. (1990). Calcium-sensitive delayed rectifier potassium currents in guinea pig ventricular cells. *American Journal of Physiology*, 258:H1200–H1207.
- Walmsley, J., Mirams, G., Bahoshy, M., Bollensdorff, C., Rodriguez, B., and Burrage, K. (2010). Phenomenological modeling of cell-to-cell and beat-to-beat variability in isolated guinea pig ventricular myocytes. In *Proceedings of the 32nd Annual International IEEE EMBS Conference 2010*.
- Wang, Z., Feng, J., Shi, H., Pond, A., Nerbonne, J. M., and Nattel, S. (1999). Potential molecular basis of different physiological properties of the transient outward  $K^+$  current in rabbit and human atrial myocytes. *Circulation Research*, 84:551–561.

Zabel, M., Koller, B. S., Sachs, F., and Franz, M. R. (1996). Stretch-induced voltage changes in the isolated beating heart: importance of the timing of stretch and implications for stretch-activated ion channels. *Cardiovascular research*, 32:120–130.